

# **Computer aided diagnosis of cerebrovascular disease based on DSA image**

Medical images processing  
Master's Degree Programme in Information and Communication Technology  
Department of Computing, Faculty of Technology  
Master of Science in Technology Thesis

Author:  
Keke Shi

Supervisors:  
MSc (Tech) Qingqing Li  
Assoc.Prof. Tomi Westerlund

June 2021

The originality of this thesis has been checked in accordance with the University of Turku quality assurance system using the Turnitin Originality Check service.

## **Master of Science in Technology Thesis**

**Department of Computing, Faculty of Technology  
University of Turku**

**Subject:** Medical images processing

**Programme:** Master's Degree Programme in Information and Communication Technology

**Author:** Keke Shi

**Title:** Computer aided diagnosis of cerebrovascular disease based on DSA image

**Number of pages:** 51 pages

**Date:** June 2021

### **Abstract.**

In recent years, the incidence of cerebrovascular diseases in China has shown a significant upward trend, and it has become a common disease threatening people's lives. Digital Subtraction Angiography (DSA) is the gold standard for the diagnosis of clinical cerebrovascular disease, and it is the most direct method to check the brain lesion. At present, there are the following two problems in the clinical research of DSA images: DSA is a real-time image with numerous frames, containing much useless information in frames; thus, human interpretation and annotation are time-consuming and labor-intensive. The blood vessel structure in DSA images is so complicated that high practical skills are required for clinicians. In the computer-aided diagnosis of DSA sequence images, there is currently a lack of automatic and effective computer-aided diagnosis algorithms for cerebrovascular diseases. Based on the above issues, the main work of this paper is as follows:

1. A multi-target detection algorithm based on Faster-RCNN is designed and applied to the analysis of brain DSA images. The algorithm divides DSA images into arterial phase, capillary phase, pre-venous phase and sinus phase by identifying the main blood vessel structure in each frame. And on this basis, we analyze the time relationship between the time phases.

2. On the basis of DSA phase detection, a key frame location algorithm based on single blood vessel structure detection is designed for moyamoya disease. First, the target detection model is applied to locate the internal carotid artery and the Willis circle. Then, five frames of images are extracted from the arterial period as keyframes. Finally, the nidus' ROI is determined according to the position of the internal carotid artery.

3. A diagnostic method for cerebral arteriovenous malformation (AVM) is designed, which combines temporal features and radiomics features. First, on the basis of DSA time phase detection, we propose a deep learning network to extract vascular time features from the DSA video; then, the time feature is combined with the radiomics features of the static keyframe to establish an AVM diagnosis model. While assisting diagnosis, this method does not require any human intervention, and reduces the workload of clinicians. The diagnostic model that combines time features and radiomics features is applied to the study of AVM staging. The experimental results prove that the classification model trained by fusion features has better diagnostic performance than the model trained by either time features or radiomics features.

Based on the above three parts, this paper establishes a cerebrovascular disease analysis framework based on radiomics method and deep learning. We introduce corresponding solutions for DSA automatic image reading, rapid diagnosis of moyamoya disease, and precise diagnosis of AVM. The method proposed in this paper has practical significance for assisting the diagnosis of cerebrovascular disease and reducing the burden of medical staff.

**Keywords:** Digital Subtraction Angiography(DSA); Radiomics analysis; Arteriovenous malformations; Moyamoya; Faster-RCNN; Temporal features; Fusion features.

# Contents

|       |   |    |
|-------|---|----|
| 1     | Introduction.....   | 2  |
| 1.1   | Overview of cerebrovascular disease .....                                 | 2  |
| 1.2   | Current Research Situation .....  | 4  |
| 1.2.1 | Machine learning in radiomics analysis .....                              | 4  |
| 1.2.2 | Research status of DSA image analysis.....                                | 5  |
| 1.3   | Main contents and innovation points of the paper .....                    | 5  |
| 2     | Machine learning in medical image analysis .....                          | 7  |
| 2.1   | Traditional machine learning methods .....                                | 7  |
| 2.1.1 | SVM .....   | 7  |
| 2.1.2 | Logistic regression model.....  | 9  |
| 2.1.3 | Decision Tree.....  | 10 |
| 2.2   | Deep learning methods.....  | 11 |
| 2.2.1 | VGG network.....  | 11 |
| 2.2.2 | Resnet network.....   | 11 |
| 2.2.3 | LSTM series .....   | 13 |
| 2.2.4 | 3D-ConvNet series.....  | 15 |
| 2.2.5 | Faster-RCNN .....   | 15 |
| 2.3   | Summary .....   | 16 |
| 3     | Time phase analysis of DSA .....  | 18 |
| 3.1   | Introduction .....  | 19 |
| 3.2   | Cerebrovascular detection and phase distinction.....                      | 20 |
| 3.2.1 | Patients and materials.....   | 20 |
| 3.2.2 | Multi-structure detection .....   | 21 |
| 3.2.3 | Temporal features.....  | 23 |
| 3.3   | Results .....   | 24 |
| 3.3.1 | Cerebrovascular detection results.....                                    | 24 |
| 3.3.2 | Phase division results .....  | 27 |
| 3.4   | Summary .....   | 28 |
| 4     | Time phase analysis in ROI detection of the moyamoya disease.....         | 30 |
| 4.1   | Introduction .....  | 30 |
| 4.2   | ROI detection of moyamoya disease.....                                    | 30 |
| 4.2.1 | Patients and material .....   | 30 |
| 4.2.2 | Automatic annotation method .....   | 31 |
| 4.3   | Diagnosis of moyamoya disease .....                                       | 33 |
| 4.4   | Results .....   | 34 |
| 4.5   | Summary .....   | 36 |
| 5     | Assisted diagnosis of AVM based on radiomics and time phase analysis..... | 37 |
| 5.1   | AVM Diagnosis .....   | 37 |
| 5.1.1 | Patients and material .....   | 37 |
| 5.1.2 | Feature extraction.....   | 38 |
| 5.1.3 | Features Selection and model building .....                               | 39 |
| 5.2   | AVM nidus staging.....  | 39 |

|   |    |
|---|----|
| 5.2.1 Patients and materials.....         | 40 |
| 5.2.2 Model building with stage.....      | 42 |
| 5.2.3 Model building with properties..... | 42 |
| 5.3 Results.....                          | 44 |
| 5.3.1 AVM diagnosis results.....          | 44 |
| 5.3.2 AVM staging results.....            | 46 |
| 5.4 Summary.....                          | 49 |
| 6 Conclusion and Future Work.....         | 50 |
| 6.1 Conclusion.....                       | 50 |
| 6.2 Future Work.....                      | 51 |
| References.....                           | 52 |
| Published Work.....                       | 56 |

# 1 Introduction

## 1.1 Overview of cerebrovascular disease

In recent years, cerebrovascular disease, as a disease that poses a threat to national health, has a high recurrence rate and disability rate. In most cases, although timely interventional treatment can reduce mortality, most patients' body functions will be damaged to a certain extent [1]. Cerebrovascular disease can be divided into ischemic cerebrovascular disease and hemorrhagic cerebrovascular disease. The risk of hemorrhagic cerebrovascular disease is much higher than that of ischemic cerebrovascular disease. Depending on the location, amount, and bleeding speed, different degrees of brain damage can be caused.

Moyamoya disease is a cerebrovascular disease of unknown etiology. The typical clinical manifestations are transient cerebral ischemia, cerebral infarction, and cerebral hemorrhage [2]. Among them, transient cerebral ischemia caused by vascular stenosis is the most common, compensating for blood vessels, with excellent bleeding risk. Cerebral arteriovenous malformation (AVM) comprises malformed vascular clusters, supply veins, and drainage veins [3]. Although only part of brain AVM patients presents with symptoms like headache or seizure, a mortality rate of 10-15% and a morbidity rate of 30-50% were reported in young adults with intracerebral hemorrhage caused by AVM [4]. In clinical manifestations, 40% to 70% of AVM are manifested as cerebral hemorrhage, and 20%-30% are manifested as epilepsy. In imaging manifestations, AVM is often accompanied by aneurysms and venous aneurysms, which is an essential reason for intracranial hemorrhage in young people [5].

The principle of DSA is to put the image with the injected contrast agents and the one without contrast agents into the computer and perform the digital subtraction, enhancement, and other processing procedures to obtain the sequence images of blood vessel. As the contrast agent flows in the cerebrovascular, the developed structure will gradually change. The number of image frames in each case depends on the length of time for vascular imaging [6]. Generally, it can be divided into four periods: arterial

period, capillary period and early venous period, and venous sinus period [7]. Compared with computed tomography angiography (CTA) and magnetic resonance angiography (MRA), DSA can dynamically and directly reflect the vascular structure instead of static simulation reconstruction, providing unique time dynamic characteristics [8]. DSA can indicate the location, extent, and scope of the lesion while displaying the arterial blood flow, thus providing an objective basis for surgery. These are reasons that why DSA is provided as the gold standard of cerebrovascular disease diagnosis, and not replaceable by other imaging technologies such as CTA/MRA.

DSA has essential value in the judgment of cerebrovascular diseases, such as moyamoya disease, arteriovenous malformations (AVM), arteriovenous fistula (DAVF), and so on. Early development of venous blood vessels in the arterial or capillary phase is an essential sign of its diagnosis. However, it might be labor- and time-consuming for inexperienced doctors to read DSA and give an accurate brain disease diagnosis. Therefore, a computer aided diagnosis system able to recognize cerebrovascular disease would help provide diagnostic hints, especially in emergency cases.

Nowadays, the technology of manufacturing and image processing of DSA equipment is quite mature. However, the research on automatic reading and diagnosis of DSA is still quite few. The diagnosis of cerebrovascular disease through angiography images mainly depends on the subjective observation of neurologists or radiologists. For physicians with insufficient clinical experience, misdiagnosis or missed diagnosis is prone to occur, or even ignoring information about lesions that should be treated. The research in computer-aided diagnosis based on machine learning has made significant progress in recent years, which can be used for tumor staging, pathological typing, prognostic evaluation, efficacy testing [9], and many other aspects.

This paper used radiomics and deep learning related methods to accurately detect and diagnose cerebrovascular disease, which are helpful to reduce the time and labor costs of physicians, and the rate of misdiagnosis. The proposed computer-aided diagnosis system of cerebrovascular disease is a valuable attempt for automatic diagnosis of cerebrovascular disease and has practical clinical value.

## 1.2 Current Research Situation

### 1.2.1 Machine learning in radiomics analysis

Radiomics combines machine learning with quantitative image analysis and is considered a technology of extracting diagnosis and treatment related information from medical images. Traditional radiomics features usually include intensity, shape, texture, and wavelet of the Region of Interest (ROI). Different medical images, such as magnetic resonance imaging (MRI), ultrasound, and computerized tomography (CT), can all be used as resources for the radiomics analysis [10]. After feature selection, feature sets with predictive value are called radiomics signature [11]. Quantitative analysis of ROI through high-throughput features can obtain valuable diagnostic, prognostic, or predictive information [12]. Deep learning is an extension of traditional artificial neural network technology. The deep learning network combines feature extraction and classifiers to form an end-to-end structure, and extracts features from a large amount of input to complete classification, segmentation, and reconstruction tasks. With the advent of high-performance processors, deep learning models have made breakthroughs in natural image recognition and have gradually applied to the medical field.

In image classification and segmentation, Ferreira-Junior et al. [13] used radiomics features to distinguish adenocarcinoma, squamous cell carcinoma, and large cell carcinoma. They obtained an AUC of 0.71 in the validation group, indicating that radiomics methods have great potential in diagnosing histopathological subtypes of lung cancer. Mehmet et al. [14] used a single 3-class U-net to segment breast and fibroglandular tissue, and the Dice Similarity Coefficient (DSC) reached 0.944. Yuan et al. [15] distinguished adenocarcinoma in situ, micro-invasive adenocarcinoma, and invasive adenocarcinoma based on CT images with radiomics. The accuracy of the radiomics method was significantly higher than that of conventional volume analysis. Marios et al. [16] used a deep neural network to perform lung pattern classification with 85.5% accuracy. In prognostic evaluation, Huang YQ et al. [17] used CT images to

realize survival prediction. Studies have shown that the predicted accuracy of radiomics on survival of patients is better than that of traditional tumor staging.

Deep learning and radiomics methods have achieved fruitful results in medical imaging research, helping doctors to make treatment decisions to a certain extent and reducing patients' risks.

### **1.2.2 Research status of DSA image analysis**

In DSA analysis research, the current study focused on image registration, image denoising, hemodynamic modeling, and blood vessel extraction. In image registration, the research is to eliminate image artifacts and enhance the intensity of blood vessels. In the hemodynamic analysis, the manual-labeled vascular structure is usually applied to extract the features for further research and analysis. Xu Zhang et al. [18] separately analyzed the ROI of frontal, parietal, temporal, and occipital lobes to calculate each period of the brain lobe's time density curve, judging the carotid artery perfusion characteristics. For blood vessel extraction, methods can usually be divided into a pattern recognition method, tracking method, waveguide method, etc. All of which need to mark the topological structure of blood vessels in advance. Most prior related research on cerebrovascular disease diagnosis is based on one or two types of high dimension medical images, like 3D MRI, 3D DRA. These study are focused on the extraction of the nidus [19,20,21]and the classification of feeding vessels and drain vessels .So far, there have been few studies about the direct diagnosis of 2D DSA, let alone DSA radiomics studies.

### **1.3 Main contents and innovation points of the paper**

Most of above studies are based on single-position DSA images. This paper mainly combines the deep learning and radiomics technique to implement the automatic computer-aided diagnosis for cerebrovascular diseases. DSA sequence images are analyzed to obtain time phase information, to locate keyframe of moyamoya, and fulfill AVM diagnosis.

First, this paper introduces the basic methods of deep learning networks and radiomics method that can be applied in the DSA video. Chapter2 will elaborate on this part.

Considering that developed vessel structures always change with time, we apply a multi-target detection model to distinguish different time phase. Also ,the time relationship between the different time phases are analyzed for further study. Chapter 3 will elaborate on this part.

On the basis of the chapter 3, we introduce the time analysis method to the DSA image analysis of moyamoya disease. Given that the keyframe extraction is time-consuming and laborious, we design a method to automatically locate moyamoya disease lesion. Chapter 4 will elaborate on this part.

To improve the diagnosis accuracy in DSA images without manual annotation, the proposed temporal features was integrated with radiomics features (grayscale features, wavelet features, texture features) for AVM diagnosis and AVM staging. For AVM staging, we also combine the radiomics features with deep features for model training. Chapter 5 elaborates on this part.

There are three innovations in this paper, which can be summarized as follows:

1. A multi-vascular structure detection model is designed for time phase analysis of DSA videos based on Faster-RCNN. This model records the vascular structure in each frame to distinguish time phase into the arterial phase, the capillary phase, the pre-venous phase and the sinus phase, which improve the DSA reading rate.
2. A feature extracted method for temporal features is proposed on the basis of time phase analysis process, which is applied to the ROI location of moyamoya disease and AVM-assisted diagnosis ,reducing the pressure of annotation work.
3. A DSA-based AVM diagnosis and staging model is proposed, combining dynamic time features with static imaging radiomics features. Given that the good result of the model, it may help radiologists to improve the diagnostic accuracy, and provide surgical options in future.

# 2 Machine learning in medical image analysis

The general process of traditional medical image analysis can be divided into feature extraction, feature encoding, feature clustering, feature selection, and model training. The underlying features are generally Histogram of Oriented Gradient(HOG), Speeded Up Robust Features (SURF), Local Binary Patter (LBP), and other features. After selecting the features, we can use traditional machine learning methods such as random forest, Support vector machine (SVM), and logistic regression for classification. In a deep neural network, you only need to input the image, and the model will automatically perform feature extraction and result mapping.

In this chapter, we will introduce a basic machine learning method suitable for DSA images study.

## 2.1 Traditional machine learning methods

### 2.1.1 SVM

SVM is a two-classification model [22,23,24],and the main idea is to find an optimal hyperplane in space that is able to divide all data samples and make the distance between data in the sample set, and this hyperplane the shortest. The equation of the hyperplane can be written as:

$$W^T x + b = 0 \quad (2.1)$$

where the average vector is  $W$ , and the offset is  $b$ . The distance between the two hyperplanes is called margin, and the maximum separation hyperplane is in this area, as shown in Figure 2-1.

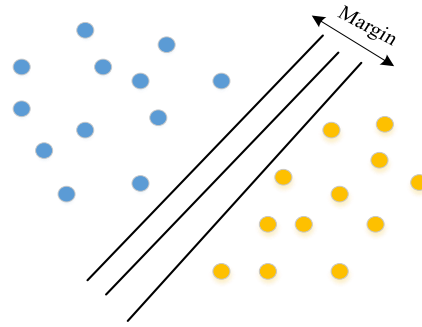


Figure 2-1 Linear separable data

The distance  $d$  from the sample point  $P(x_1, x_2, \dots, x_n)$  of the data set to the hyperplane is:

$$d = \min_{w, b} \frac{1}{2} \|W\|^2$$

(2.2)

Since each hyperplane can correspond to a margin, the objective function for finding the maximum interval hyperplane can be written as:

$$\arg \max_{w, \sigma} \left\{ \min(y(w^T x + b)) \cdot \frac{1}{\|w\|} \right\} \quad (2.3)$$

For linearly separable data, the sample point of the training set, the closest to the hyperplane, is called support vectors. Nonlinearly separable data cannot find a hyperplane that can completely separate the two types of data, as shown in Figure 2-2. To minimize the sample points that do not meet the conditions, a penalty term for these points will be added to the objective function. The objective function can be written as:

$$\min_{w, b} \frac{1}{2} \|W\|^2 + C \sum_{i=1}^n \max(0, 1 - y_i (X_i^T W + b)) \quad (2.4)$$

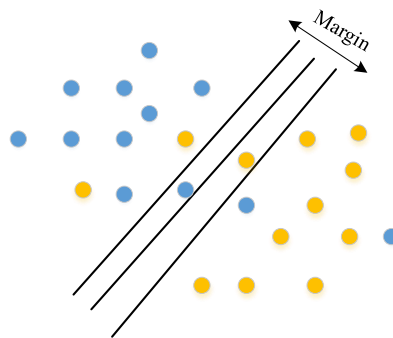


Figure 2-2 Non-linear separable data

For nonlinear problems, use kernel trick to convert linear support vector machines into nonlinear support vector machines. We map the sample points to the high-dimensional

space in a certain way, so that the non-linearly separable sample points are linearly separable in the high-dimensional space. The inner product in the linear support vector machine is replaced by the kernel function [25,26], and the nonlinear support vector machine can be obtained. The standard kernel functions are as follows, as shown in Table 2.1.

Table 2.1 Kernel function

| Kernel function   | Function Expression                          |
|-------------------|--|
| Linear kernel     | $k(x, y) = x^T y$                            |
| Polynomial kernel | $k(x, y) = (\alpha x^T y + c)^\delta$        |
| Gaussian kernel   | $k(x, y) = \exp(-\frac{(x-y)^2}{2\sigma^2})$ |
| Exponent kernel   | $k(x, y) = \exp(-\frac{(x-y)}{2\sigma^2})$   |
| Laplace kernel    | $k(x, y) = \exp(-\frac{(x-y)}{\sigma})$      |
| Sigmoid kernel    | $k(x, y) = \tanh(\alpha x^T y + c)$          |

The SVM algorithm has a simple structure and good robustness. It is suitable for small sample learning methods, so it has a good application prospect in the medical field with limited data.

### 2.1.2 Logistic regression model

Logistic regression is a generalized linear regression analysis model [27]. The steps of establishing a regression model can be divided into constructing hypothesis function, constructing loss function, and optimizing loss function. The hypothesis function is:

$$h(x) = \sum_{i=0}^n \theta_i x_i = \theta^T x + b \quad (2.5)$$

where  $h(x)$  is the target value,  $\theta_i$  is the influencing factor, and  $b$  is the offset. When  $g(z)$  is closer to 0, the possibility of indicating 0 is greater; when  $g(z)$  is closer to 1, the possibility of indicating 1 is greater. Therefore, the hypothesis function of logistic regression can be expressed as:

$$h_{\theta}(x) = g(\theta^T x) = \frac{1}{1 + e^{-\theta^T x}} \quad (2.6)$$

We assume that the output value of the function is as close to 0 or 1 as possible. For a single sample of data, the posterior probability formula can be written as:

$$P(y | x; \theta) = (h_{\theta}(x))^y (1 - h_{\theta}(x))^{1-y} \quad (2.7)$$

$$L(\theta) = \prod_{i=1}^m p(y_i | x_i; \theta) = \prod_{i=1}^m (h_{\theta}(x_i))^{y_i} (1 - h_{\theta}(x_i))^{1-y_i} \quad (2.8)$$

We obtain the partial derivative of the likelihood function. In this way, the direction of gradient ascent in each update iteration can be obtained. In logistic regression, the gradient ascent method is used to find the optimal solutions.

In logistic regression, it is easy to observe the probability scores of samples. Although the logistic regression is easy to be used and understand, it is prone to be under-fitting in the training process and cannot handle samples with large feature spaces well.

### 2.1.3 Decision Tree

A decision tree is, composed of directed edges and nodes [28]. The nodes are divided into two types: internal nodes and leaf nodes. Leaf nodes represent classes, and internal nodes represent features. The basic idea is to use information entropy to construct a tree with the fastest decline.

The core of the ID3 algorithm [29] is to use information gain for feature selection. The information gain expression is  $I(D,A)$ , where  $D$  is the sample input set, and  $A$  is the feature set. The C4.5 algorithm [30] discretizes continuous features to solve the problem that ID3 cannot handle the continuous values. First, the dataset with missing features and corresponding feature values are solved by calculating the weighted information gain ratio. Then, it divides the sample with missing values into all the child nodes simultaneously and distributes the weight of the sample. The CART algorithm [31] can solve classification problems and be applied to regression problems and simplifies the calculation of the model which uses the Gini coefficient instead of the information gain ratio. The expression of the Gini coefficient can be written as:

$$Gini(D) = 1 - \sum_{k=1}^K \left( \frac{|C_k|}{|D|} \right)^2 \quad (2.9)$$

where  $D$  is a given sample and  $C_k$  is the number of the  $k$  category.

The decision tree algorithm is very intuitive and easy to be explained. There is no need to deal with missing values in data processing. However, the decision tree is prone to overfitting and can be easily affected by sample changes.

## 2.2 Deep learning methods

### 2.2.1 VGG network

VGG network [32] emphasizes depth in convolutional neural networks. The central idea of VGG is to improve network performance by increasing the depth of the network, and decrease the parameters by reducing the size of the convolution kernel. After each convolution, the size of the feature map is kept unchanged. After each pooling, the depth of feature map is reduced by half. VGG fills in the image's edge to keep the convolution input and output size consistent, and retains sufficient information of the image edge. It only uses the pooling unit to reduce the image's size, simplify and optimize network parameters' design.

VGG is a suitable feature extractor, and the trained model is often applied to transfer learning. Its network structure and design method have inspired many deep learning networks today.

### 2.2.2 Resnet network

As the number of network layers increases, the accuracy will reach saturation or even decline. To solve these problems, K. He et al. proposed the method of residual learning [33]. It is achieved by establishing identity mapping and the residual learning unit, which is shown in Figure 2.3. It can be written as:

$$y = F(x, \{W_i\}) + x \quad (2.10)$$

where  $x$  is identity mapping.

Theoretically, if the model is at the optimal state and can be optimized to 0, no matter how the depth is increased, the model will always be optimal. There are five primary forms of Resnet: Res18, Res34, Res50, Res101, Res152. The residual block in Figure 2-3(a) is generally used for shallow networks, such as Res34. The residual block in Figure 2-3(b) is generally used for deep networks, such as Res101 and Res152, which are called bottleneck designs. The primary purpose is to reduce the network dimension and the amount of calculation and parameters.

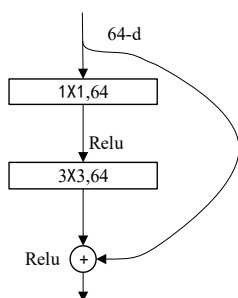


Figure 2-3(a) Residual block

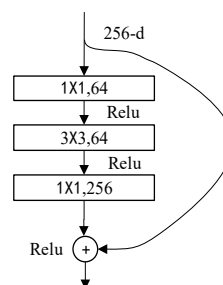


Figure 2-3(b) Bottleneck design

As shown in Figure 2-4, the network consists of three main parts: input part, output part, and intermediate convolution part. Although the forms of Resnet are diverse, they all follow the above-mentioned structural characteristics. The difference between networks is due to differences in the block parameters and numbers of the intermediate convolution part.

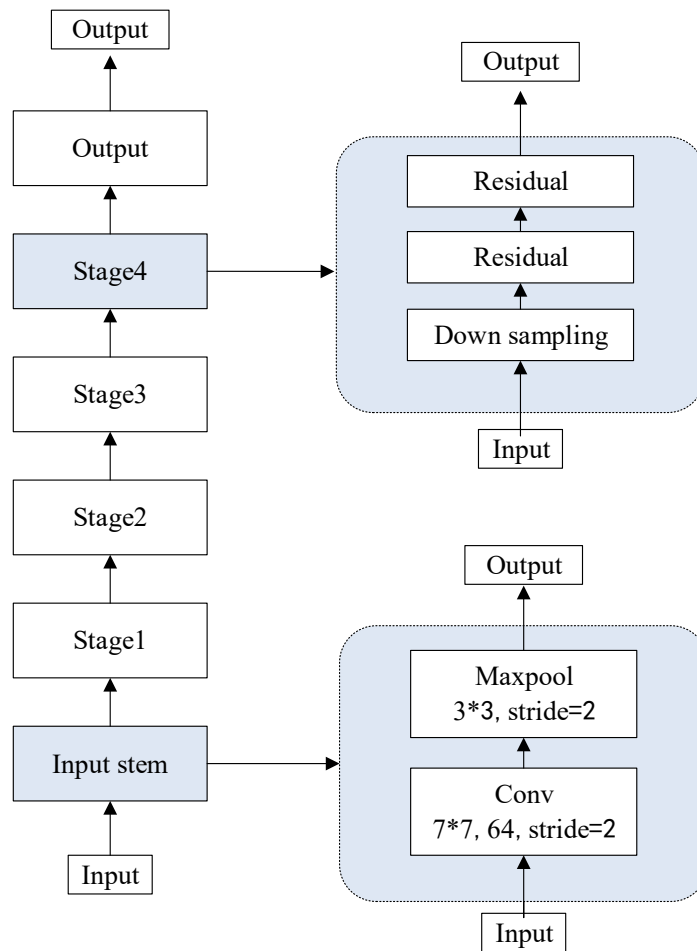


Figure 2-4 Structure of Resnet

### 2.2.3 LSTM series

Long Short Term Memory Network (LSTM) is a time loop neural network [34], which is usually applied to time-delayed events. The basic cyclic unit in LSTM is called cell, which is composed of three parts: forget gate, input gate, and output gate. The structure diagram is shown in Fig 2.5. The forget gate, which determines how much of the state at the previous moment  $c_{t-1}$  is retained to the current moment  $c_t$ . The input gate, which determines how much of the network's input  $x_t$  is saved in the current state  $c_t$ .

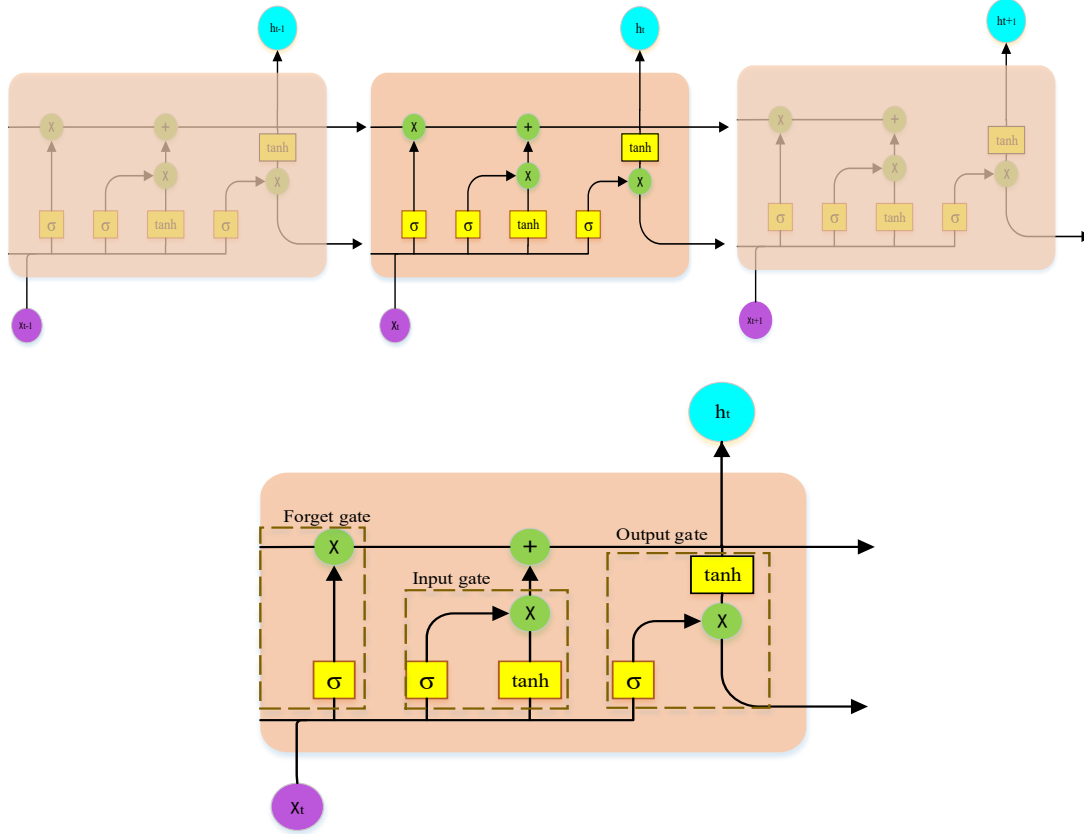


Figure 2-5 structure diagram of LSTM

The function of a gate is equivalent to a fully connected layer, which controls the state through an activation function. The forget gate determines what information should be discarded from the cell. The sigmoid layer determines the cell output, where 0 means that the information is completely forgotten, and 1 means that the information is completely retained. The input gate determines which information is valid and stored in the current state. The corresponding formula is:

$$f_t = \sigma(W_i \cdot [h_{t-1}, x_t] + b_i) \quad (2.11)$$

$$\tilde{c}_t = \tanh(W_c \cdot [h_{t-1}, x_t] + b_c) \quad (2.12)$$

$$c_t = f_t \cdot c_{t-1} + i_t \cdot \tilde{c}_t \quad (2.13)$$

where  $W_i, W_c$  are the weight matrix,  $h_t$  is the hidden layer of current state,  $b_i, b_c$  are the bias term, and  $\tilde{c}_t$  is the state of the current door. The output gate determines the output, which is based on the current cell state.

Long-term Recurrent Convolution (LRCN) is a network that combines LSTM and CNN to classify video images [35]. It extracts the apparent information of the video frame

through the CNN layer, and the LSTM layer retains the information of the time dimension, which help the network to obtain spatial and temporal features well.

### 2.2.4 3D-ConvNet series

The 2D convolution operation performs a sliding window operation on the input image by the convolution kernel to obtain the feature map of the next layer. To preserve the timing information between frames, the C3D network extends 2D convolution to 3D convolution and adjusts the convolution kernel to increase the one-dimensional time-domain depth [36], as shown in Figure 2-6.

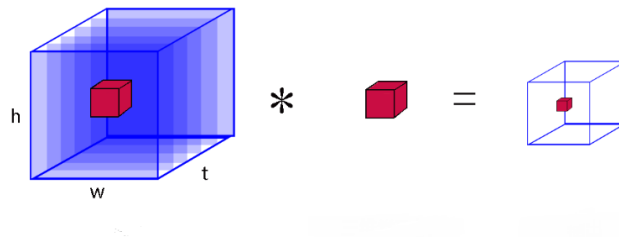


Figure 2-6 3D convolutional

I3D is an improved version of C3D. Its innovation lies in the weight initialization of the model [37], which assigns the weights of pre-trained 2D ConvNets to 3D ConvNets. But, compared with traditional 2D convolution, the parameters of the 3D convolution model are cubic levels of the 2D convolution, which will influence the training of the network. To optimize the operating speed and reduce the number of parameters of the C3D network, P3D is proposed. It expands Resnet to a pseudo 3D convolution [38], which uses a  $3 \times 3$  and three  $1 \times 1$  convolution instead of 3D convolution and retain the advantages of C3D network.

### 2.2.5 Faster-RCNN

In recent years, target detection models ,based on deep network, have achieved

significant results. The most popular two-stage model, Faster RCNN [39], involved in the thesis, will be introduced.

In Faster-RCNN model, the feature extraction module usually uses Resnet or VGG network as the base bone. Resnet uses a "short connection" strategy to provide a propagation channel for the gradient, which solves the problem that the gradient decreases as the network depth increases.

Faster-RCNN is composed of feature extraction module, Regional Proposal Network (RPN) module, ROI Pooling module and classification regression module. The regional prediction network (RPN) can be divided into three parts. In the head of the RPN, anchors are generated. In the middle of the RPN, there are two branches in there, one is the classification branch, and the other is the bounding box regression branch which calculates the coordinate bounding box that generated by the head. The classification branch uses the softmax layer to obtain the foreground and background, and the bounding box regression branch obtains the regression offset. In the end of the RPN, it will remove the bounding box that does not meet the conditions. According to the classification results, the non-maximum suppression (NMS) algorithm is applied to deduplicate, which realizes the preliminary selection of the anchors generated by the head.

The ROI-Pooling part collects the output feature map of convolutional layer and the candidate area output by the RPN. It unifies the feature map with the size of the output area so that a fixed size feature map can be obtained, and finally the features are sent to the full connection layer.

The classification regression module uses the features extracted from the target area to identify the image and uses bounding box regression to obtain the target's precise location.

## **2.3 Summary**

In this chapter, we briefly introduced the machine learning method in medical image analysis, including traditional machine learning and deep learning algorithm.

Most classic methods are not suitable for DSA video. There are three reasons: First, the

number of DSA frames is not fixed, usually within 20 to 50 frames. The development status of each frame is related to the patient's blood flow rate and the shooting interval of the machine. In other words, when randomly selecting frames from each case, the change of the image in the time dimension will be different. Secondly, there are interference, noise, and artifacts that influence the image quality, so it is difficult to obtain effective information. Finally, the number of DSA data is limited in our research, which makes it hard to meet the conditions of deep learning networks.

To solve these difficulties, we explore the analysis process for DSA classification task. The third chapter provides the time phase analysis method of DSA, involving the vessel structures detection , which provides the basis of further study; the fourth chapter introduces a lesion location method based on time phase analysis process. The fifth chapter is about the AVM diagnosis and AVM staging, where the radiomics features and time features are combined in classification task.

## 3 Time phase analysis of DSA

DSA is the gold standard for the diagnosis of cerebrovascular diseases. The sequence of blood vessel development with contrast agents and the structure of blood vessels are the basis for diagnosing vascular diseases such as arteriovenous malformation(AVM) and moyamoya disease. The DSA video provides dynamic information and static information, which is potential for the feature analysis.

The traditional video classification usually uses apparent and temporal features for classification tasks. The preferred temporal features include spatial-temporal interest points, histogram of optical flow, dense-trajectories [40,41,42]. DSA images and videos of natural scenery have similarities in that they can reflect the target's state within a period. However, the difference is that natural videos are usually RGB images with various objects. In contrast, the DSA images are grayscale, reflecting the cerebrovascular periodical changes with limited and unfixed frames. In target detection task, traditional methods generally use a window to extract features and classify objects into different categories [43]. The specific method is to slide the proposal area through the multiple-scale sliding window and then extract features of region of interests (ROI), finally use classifiers to complete the tasks. Dalal et al. proposed a histogram of oriented gradient (HOG) features to solve pedestrian detection in static images [44]. Felzenszwalb et al. used HOG combined with SVM for target detection [45]. Most classic methods are not robust enough on the image with varying target diversity.

In this chapter, we introduced a method to analyze the dynamic information from DSA images. First, we proposed a multi-target detection model to distinguish DSA time phase, and then analyzed time distribution of different phases. Finally, we proposed a method to obtain temporal features between frames automatically. This algorithm had promoted speed of the DSA reading, shortened the reading time, and reduced the human labor cost and the rate of misdiagnosis.

### 3.1 Introduction

In clinical study, DSA can be roughly divided into five phases: pre-arterial phase, post-arterial phase, capillary phase, pre-venous phase, and sinus phase. In arterial phase, internal carotid artery, middle cerebral artery and anterior cerebral artery and their proximal branches are presented. Venous phase is characterized by several venous sinuses, including superior sagittal sinus, inferior sagittal sinus, sigmoid sinus and straight sinus and transverse sinus, etc. And capillary phase is the transitional period between arterial and venous phase, characteristic of distal arterial branches and capillary arteries.

Fig.3.1 shows the trend of standard cerebral angiography. Given that lesion locations will influence the perfusion time and phase of main vascular structure, multi-position of the DSA images should be considered to give the final diagnosis. Thus, doctors need to observe the distribution of the vascular structure in each phase, which is time-consuming and laborious. Dynamic flow information of the cerebrovascular arterial tree is provided with excellent visualization, which makes the detection of cerebrovascular structure possible. Portions of text and figures of this chapter are reproduced from our previous works [48].

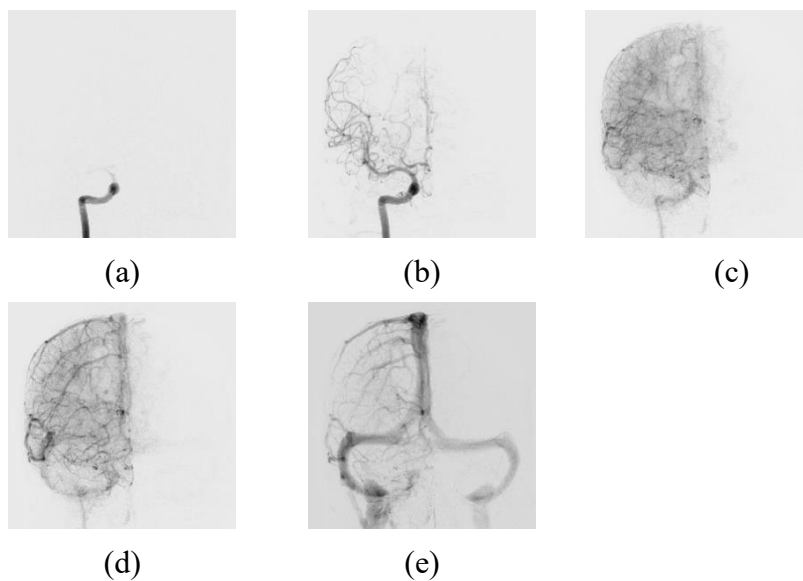


Fig 3.1 Different phase of normal DSA image. (a) Early arterial phase;(b) Late arterial phase. (c) Capillary phase;(d) Early venous phase;(e) Venous sinus phase.

## 3.2 Cerebrovascular detection and phase distinction

### 3.2.1 Patients and materials

A total of 191 patients with the intra-arterial position from January 2010 to December 2013 was collected in this study. 153 cases were used in model training, and 38 cases was applied in time phase analysis. The research protocol was reviewed and approved by the Huashan Hospital ethics committee. Specialist doctors, who have been engaged in clinical cerebrovascular disease for more than five years, selected normal anteroposterior position (AP) and marked the critical structures of blood vessels in different periods. If there was any ambiguity, the third senior doctor would read and finalize it. A total of five structures was marked in different phases, shown in Fig.3.2.

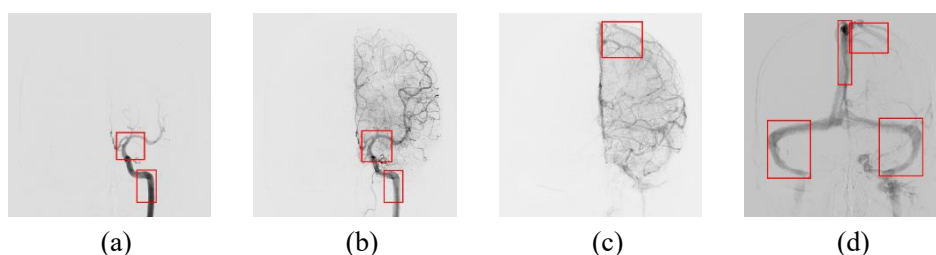


Fig. 3.2 The annotation of different phase; a. Early arterial phase. b. Late arterial phase .  
c. Early venous phase. d. Late venous phase.

Among 153 patients, 4 or 5 frames were selected from each case and a total of 680 images were collected. After ROI annotation, there were 326,334,350,346,362 annotation boxes on the internal carotid artery, the Willis circle the large vein, the venous vessel, and the venous sinus, respectively. We saved the vessel category and the coordinate position in the corresponding XML file, which would be transferred to VOC2007 form.

The VOC2007 data set contained three folders, *Annotations*, *JPEGImages*, and *ImageSets*. The *Annotations* folder stored the XML file that was corresponding to each image, *JPEGImages* stored all the images, and the *ImageSets* folder stored the TXT

files that recorded the name of training set and test set images. We set the training set to 80%, and the test set to 20%. The details of the data set were shown in Table 3.1.

Table 3.1 Data summaries

|                | Category       | Training set | Test set | Total |
|----------------|----------------|--------------|----------|-------|
| Annotation num | Carotid artery | 260          | 62       | 326   |
|                | Willis circle  | 267          | 67       | 334   |
|                | Vein           | 280          | 70       | 350   |
|                | Venous Vessel  | 276          | 70       | 346   |
|                | Venous sinus   | 289          | 73       | 362   |
|                | Total          | 1372         | 342      | 1714  |

### 3.2.2 Multi-structure detection

We conducted a target detection algorithm, Faster-RCNN, to obtain DSA sequence information. First, the annotated samples were made into VOC2007 format that met the operation condition of Faster-RCNN. Then, the Resnet50 was regarded as the base bone of Faster-RCNN to extract image features. Finally, we selected an optimal model to detect main structure and distinguish time phase in test set. The overall structure of Faster-RCNN is shown in Fig.3.3, and the basic principle could be referred in section 2.2.5. The time analysis process based on Faster-RCNN was shown in Fig. 3.4.

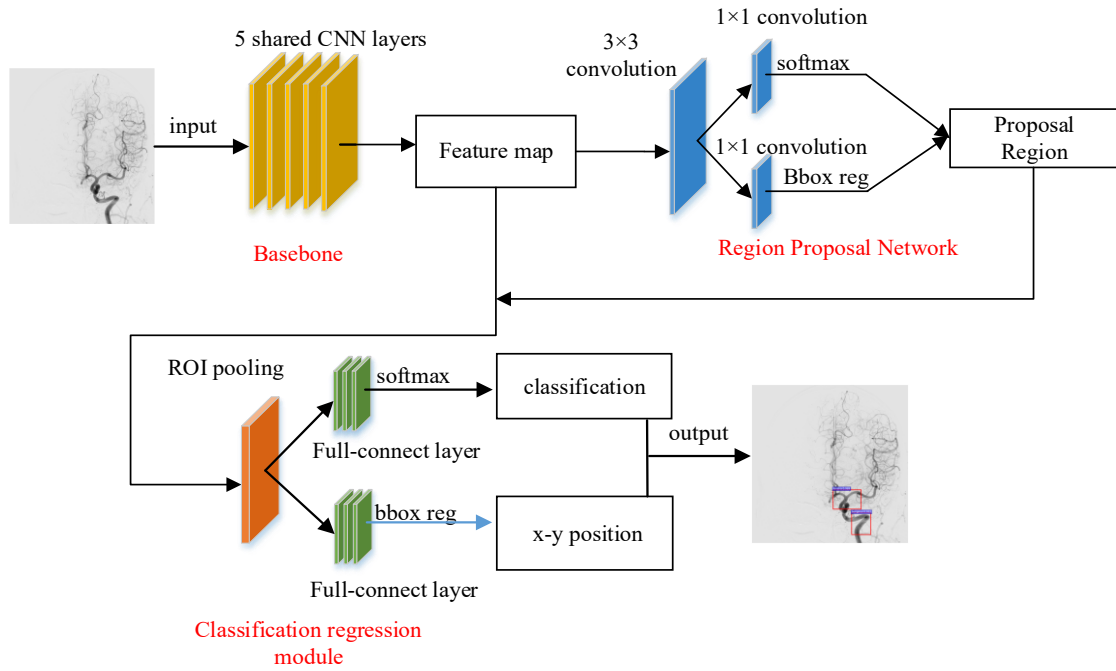


Fig.3.3 Faster-RCNN module

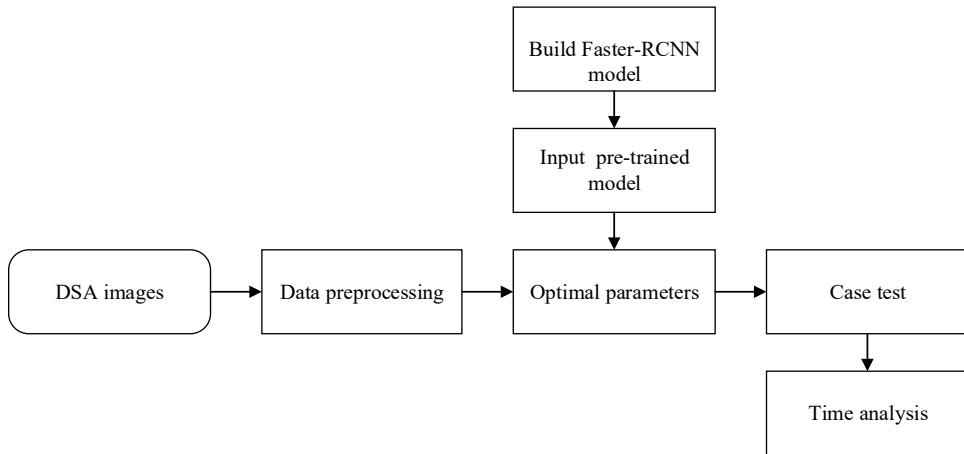


Fig.3.4 The flow chart of algorithm

After we got the optimal detection model, the result of test set would be analyzed. We applied Average Precision (AP), mean Average Precision (mAP), and Intersection-over-Union (IoU) to evaluate the performance of detection model. They were common evaluation index for multi-target detection. The IoU referred to the degree of overlap between the candidate box and the original marked box. The AP referred to the area under the Precision-Recall curve. AP evaluated the performance of the trained model in a single category. The mAP referred to the average of AP values that evaluated the

performance of the trained model in all categories,

The confidence of each coordinate bounding box was judged by the value of the intersection-over-union (IoU). if IoU was less than 0.3, the confidence of the anchor box was 0, a negative sample; if the IoU was greater than 0.7, the confidence of the anchor box was 1, a positive sample; if the IoU was between 0.3 and 0.7, it was not considered in the loss function.

### **3.2.3 Temporal features**

We could classify the time phase of DSA images by recording the types and order of cerebrovascular structures, and thus doctors set these rules: the image that can only detect the internal carotid artery and the circle of Willis is defined as the arterial phase image; the image, where no apparent blood vessels are detected, is defined as the capillary phase image; the image with large veins and without the sinuses is defined as the image pre-venous images; the image with both large veins and sinuses is defined as sinus images.

By this criterion, DSA images were divided into four phases: the arterial phase, the capillary phase, the venous phase, and the sinus phase, and each phase can be divided into early phase and later phase. Then, we put the 38 original DSA into the optimal detection model and the model will detect the cerebrovascular structures in each frame. In this way, we could get the relationship of the developed structure, which was defined as time features. The work flow of obtaining temporal features was shown in Fig.3.5, and the details of the proposed five time-sequence features were summarized in Table 3.2.

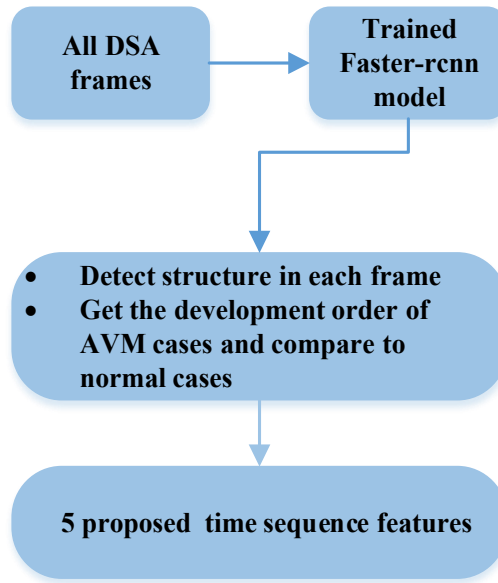


Fig.3.5 The process of obtaining temporal features

Table 3.2 The proposed 5 time features

| # | Feature | Description  |
|---|---------|--|
| 1 | T1      | Venous sinuses appear before the end of the artery                       |
| 2 | T2      | Venous sinuses appeared before the disappearance of the circle of Willis |
| 3 | T3      | Venous sinuses appear before venous vessels                              |
| 4 | T4      | Veins appear before wills ring disappeared                               |
| 5 | T5      | No obvious capillary phase   |

### 3.3 Results

#### 3.3.1 Cerebrovascular detection results

Portions of text and figures of this chapter are reproduced from our previous works

[48].The target detection model is generally trained on a fixed class, so the model needs to locate the target position in the image and classify the target category. We defined the following paramters.TP: A positive sample is predicted to be a positive sample; FN: A negative sample is predicted to be a negative sample; FP: A negative sample is predicted to be a positive sample; TN: A positive sample is predicted to be a negative sample. The definition of precision and recall are as follow:

$$\text{Precision} = \frac{TP}{TP + FP} \quad (3.1)$$

$$\text{Recall} = \frac{TP}{TP + FN} \quad (3.2)$$

Based on the predicted results, we calculated the Precision-Recall(P-R) curve of the five types of blood vessel ROI and calculated the area under the P-R curve (Average Precision) to measure the model's detection precision of each blood vessel structure. We used the target detection model to calculate the AP values of the internal carotid artery, the Willis circle, large vein, venous blood vessel, and venous sinus respectively. The results were shown in Fig.3.6. In test set, the AP of the vein was 0.889, of the internal carotid artery was 0.922, of the circle of Willis was 0.991, of the venous sinus was 0.929, and of the venous blood vessel was 0.769.

The model had a good performance in discriminating the circle of Willis and deficient in discriminating veins. The mAP of the five types of blood vessels, detected by this model, was 0.902. We can conclude that this model had a good performance on the detection of the vascular structure based on the DSA video.

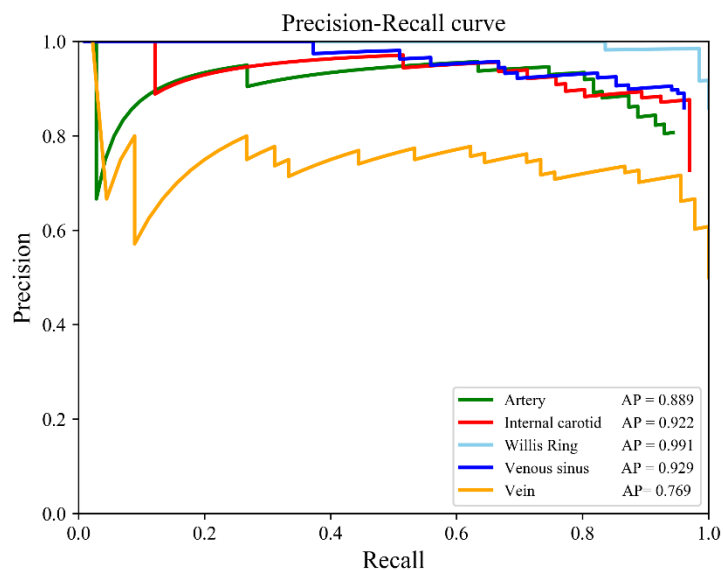
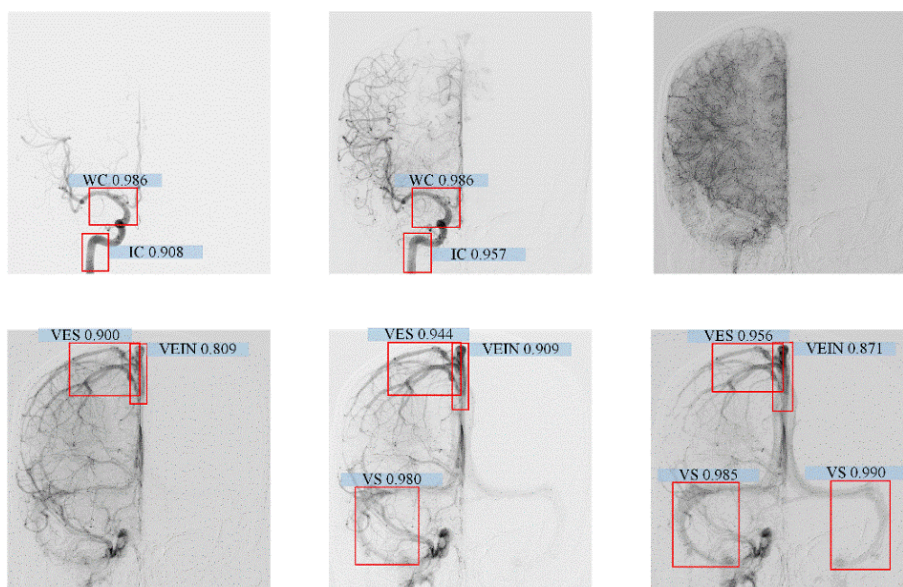


Fig3.6 P-R curve of five structure and AP value of each structures. The AP of the vein is 0.889, of the internal carotid artery is 0.922, of the circle of Willis is 0.991, of the venous sinus is 0.929, and of the venous blood vessel is 0.769

Then, we visualized the detection results of the representative images. The model can detect the positions of the internal carotid artery and the circle of Willis in the arterial phase images, as shown in Fig.3.7 (a), 3.7 (b). The positions of large veins, venous blood vessels, and venous sinuses can be detected in the venous phase images, as shown in Fig.3.7(d), Fig.3.7 (e), and Fig.3.7 (f). The capillary phase was shown in Fig.3.7(c); there was no obvious vascular structure that can be detected.



WC: Wills circle, IC: Internal carotid, VES: Venous blood vessels, VEIN: Large vein, VS: Venous sinus

Fig.3.7 Detecting results of DSA images with different phase.

### 3.3.2 Phase division results

We recorded the last frames in each phase by the type of detected structures. In independent test set, the arterial phase achieved an accuracy of 100%, the capillary phase early venous phase obtained an accuracy of 92.1%, and the accuracy of venous sinus phase was 78.9% (Table 3.3), which proved our method was significant in dividing the DSA into the arterial phase, the capillary phase, and the early venous phase. However, the venous sinus phase accuracy was relatively low. Given that the developed vessel was not apparent at the early stage of the venous sinus phase, resulting in poor accuracy.

Table 3.3 Phase classified results

| Phase              | Correct case | Wrong case | Accuracy |
|--------------------|--------------|------------|----------|
| Arterial phase     | 38           | 0          | 100.0    |
| Capillary phase    | 35           | 3          | 92.1     |
| Early venous phase | 35           | 3          | 92.1     |
| Sinus phase        | 30           | 8          | 78.9     |

Based on the vessel structure detection results, we deleted the undeveloped images, and the obtained frame delay information from the DICOM file. The time delay of the arterial phase, capillary phase, early venous phase, and venous sinus phase can be calculated respectively. The overall time distribution of 38 cases was shown in Fig.3.8.

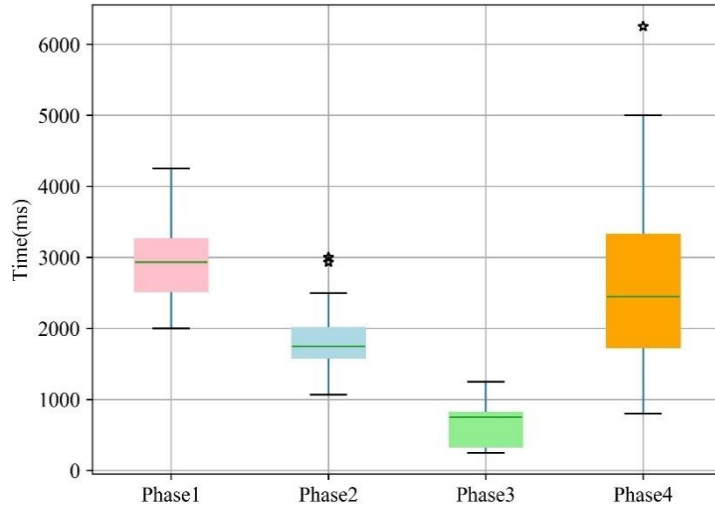


Fig3.8 Time distribution of arterial phase(phase1), capillary phase(phase2), early venous phase(phase3), and sinus phase(phase4)

This study combined structural information and time information to recognize the DSA phase automatically. On the test set, the internal carotid artery, the circle of Willis, great vein, venous blood vessel, and venous sinus achieved the AP of 0.922, 0.991, 0.899, 0.769, 0.929, respectively, and the mAP of the five types of vascular areas was 0.902.

### 3.4 Summary

In this chapter, we introduced a time phase analysis method for DSA video. Firstly, a multi-vascular structure recognition method was proposed. This method could be divided into two parts: the vessel structure recognition part, and the time analysis part. In the first part, an average accuracy of 90.2% was achieved in vascular recognition, which can accurately locate critical vascular structures. In the second part, the four

periods' average accuracy reached 90.8%, significantly reducing the length of reading time. Secondly, on the basis of vessel detection, an auto-process was proposed to obtain five time features based on Faster-RCNN.

Although Faster-RCNN might make mistakes in the structure detection of abnormal cases, we took the structure detection results of all frames into consideration when defining the time features. Therefore, if one or two frames were detected incorrectly during the whole process, it would not affect the final obtained time features.

This research still has certain limitations. First of all, this method has specific requirements on DSA images' quality, and it would reduce the detection accuracy in images with unclear blood vessel structures. Due to the limited data conditions, it is necessary to expand the dataset of this study to improve reliability of our proposed model in future.

# 4 Time phase analysis in ROI detection of the moyamoya disease

## 4.1 Introduction

Since the location of moyamoya lesions is relatively fixed, moyamoya disease can be diagnosed by the single anterior position of the internal carotid artery. The current difficulty in the diagnosis of moyamoya disease is that manual reading is time-consuming and laborious. For small volume lesions, A senior doctor is required to read the DSA to ensure a low misdiagnosis rate. The advantage of machine learning is that it can repeat the work continuously and maintain stable accuracy.

For higher resolution images, the mathematical morphology method is usually applied to image processing [46]. We can get the general shape of the blood vessel in the DSA image, and then determine the location of the lesion development. However, this method is greatly affected by noises and cannot be widely used in DSA.

In this chapter, we proposed an automatic location detection algorithm based on Faster-RCNN for moyamoya lesions. In order to determine the accuracy of ROI, we made an auto-labeled data set and a manual-labeled dataset, and then sent them to the same network, and finally verified the accuracy of the annotation by comparing the results of the model.

## 4.2 ROI detection of moyamoya disease

### 4.2.1 Patients and material

Three hundred and fifty four patients' DSA (internal carotid artery, anteroposterior position) were collected, including 62 moyamoya disease, 77 moyamoya syndrome, and 38 non-moyamoya cerebrovascular diseases, from September 2015 to October 2018 in Huashan hospital. In total, 354 hemispheres including 201 moyamoya and 153 non-moyamoya hemispheres were enrolled.

In the manual-labeled dataset, four consecutive images were selected as a sample in the arterial phase by doctors, and marked the whole lesions on each image. In the auto-labeled dataset, the location model would recognize the start and end of the arterial phase, then selected four images and annotated the lesions ROI on them.

### 4.2.2 Automatic annotation method

In this section, we introduced 2 methods for ROI detection. One was based on traditional image processing, and the other was based on deep learning.

In the traditional method, we applied the opening and closing operation in the blood vessel extraction to obtain the largest blood vessel connected domain  $S$ , which was regarded as the main blood vessel. Then extracted the centerline of the main blood vessel  $L$  [47]. Finally, by performing the above operations on each frame, the length increment  $dL$  and the area increment  $dS$  were obtained, and the additional blood vessel width  $dw$  can be calculated as:

$$dw = \frac{dS}{dL} \quad (4.1)$$

we counted the first maximum value of the  $dw$ , and regarded the frame as the initial frame. The overall flowchart was shown in Fig.4.1. However, this method had poor detection effect on images with inconspicuous lesions, and had high requirements for image quality and blood vessel distribution. Therefore, it cannot produce a large number of usable datasets for model training.

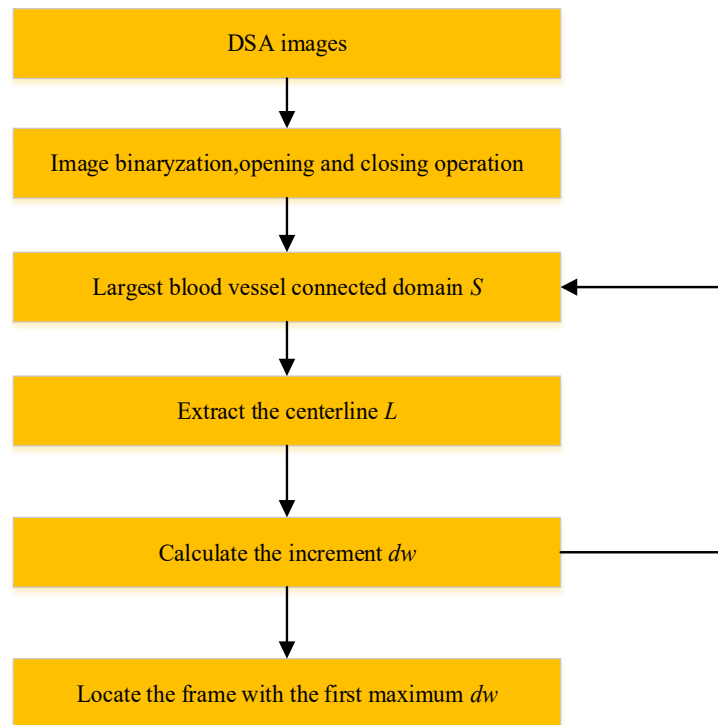


Fig.4.1 The flowchart of traditional location method

In our proposed method, ROI location task can be divided into two steps, the first step is to locate the keyframe, and the second step is to locate the lesion area. Considering that lesion frame always appears in the arterial phase, so it is necessary to determine the starting frame of the arterial phase. From the results of time phase analysis in the previous chapter, we can get the accurate arterial period by locating developed Willis circle and the internal carotid artery. On this basis, a lesion-location method for moyamoya disease was proposed, which improved the reading efficiency of DSA images and reduced the diagnosis burden of doctor.

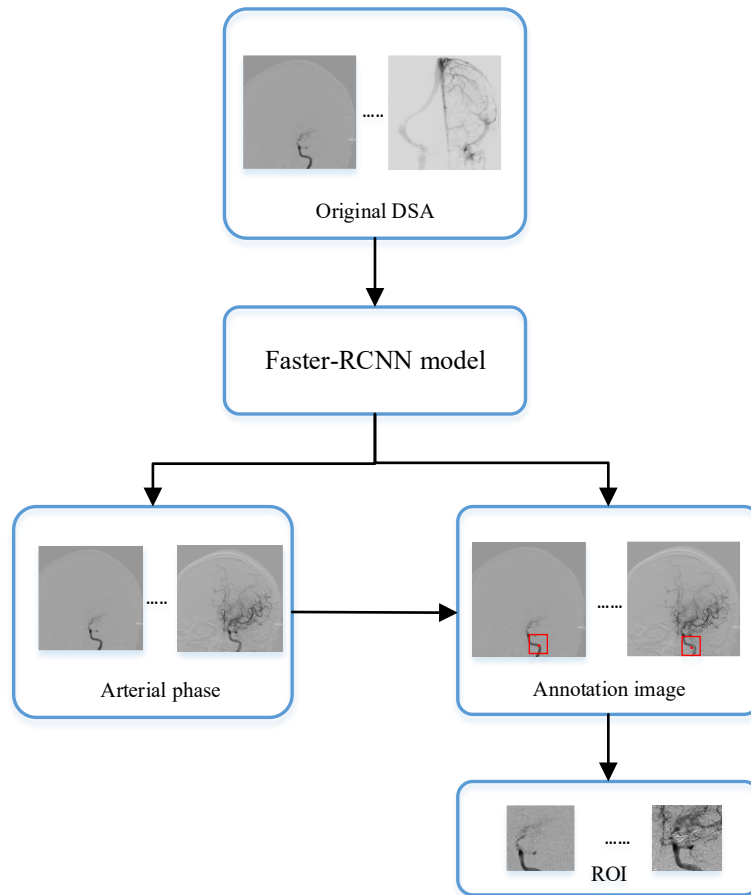


Fig.4.2 The flowchart of our proposed method

Since moyamoya lesions usually appear near the Willis circle and were easy to be located, we could use the position information of the internal carotid artery as a reference to mark the lesion area. The steps were as follows: first, we inputted the image into the target detection model. Then, obtained the position of internal carotid artery to get the central point of detected box. Finally, we regraded the central point as the boundary point to expand the ROI. The flowchart was shown in Fig. 4.2.

### 4.3 Diagnosis of moyamoya disease

To verify the accuracy of our location results, we used manual annotation method and automatic annotation method to make a comparative dataset for the same data batch respectively. In the manual annotation, the ROI size of each case changed with the lesion size, including entire lesion information. In the case of automatic annotation,

ROI size was fixed, and it was difficult to contain the whole lesions. Therefore, we extracted four frames from the arterial phase of each DSA in equal proportion and extended a size of  $300 \times 300$  to label the lesion area. After the dataset was made, we randomly divided the dataset into train set and test set with a ratio of eight to two. Then, we trained two diagnosis models based on 3D-CNN and LRCN to evaluate the accuracy of test set.

## 4.4 Results

In traditional method, 53 hemispheres with noises were excluded, and a total of 148 moyamoya samples was used in this study. We compared the difference between manual selection and algorithm identification of keyframes in each sample. The recognition result whose error was within  $\pm 2$  frames was regarded as the correct result, and exceeding 3 frames was regarded as the wrong result. According to statistical results, it could accurately identify 50% of the lesion keyframe, and the identification error within the  $\pm 2$  frames accounted for 95.9% (Table 3.1). Although the detection error was in an acceptable range in this method, it lacked robustness and required high quality of images. It cannot be applied to all DSA images.

Table 3.1 The keyframe location error statistics in traditional method

| Error margin / frame | Sample numbers | Percentage / % |
|----------------------|----------------|----------------|
| 0                    | 75             | 50.6           |
| $0 \sim \pm 1$       | 135            | 91.2           |
| $0 \sim \pm 2$       | 142            | 95.9           |
| $3 \sim 10$          | 6              | 4.1            |

In our proposed method, we have proved in chapter 3 that it had 100% accuracy in distinguishing the arterial phase. To test the ROI accuracy, we separately put the manual-labeled dataset and the auto-labeled dataset into the deep networks and analyzed the results respectively.

In this part, a total of 201 moyamoya hemispheres was applied in this study. We used two common video classification networks to classify the moyamoya disease. We also

explored the impact of image preprocessing methods on final model results. The preprocessing methods include Gaussian mean filtering (GF), gray normalization (GLN), and histogram equalization (HE). The accuracy of the test set in the two experimental groups was shown in Table 3.2. The specific principles of the 3D-CNN and LRCN network were shown in chapter 2.

Table 3.2 The accuracy of different method

|                   | Network | Non-treated | GF+GLN | GF+HE |
|-------------------|---------|-------------|--------|-------|
| Manual-annotation | 3D-CNN  | 0.82        | 0.95   | 0.91  |
|                   | LRCN    | 0.86        | 0.96   | 0.91  |
| Auto- annotation  | 3D-CNN  | 0.87        | 0.93   | 0.93  |
|                   | LRCN    | 0.88        | 0.90   | 0.91  |

In 3D-CNN, the convolution and pooling layer was a 3D mode, resulting in more parameters, and more network parameters, that would lead to the lower convergence of the loss function and training speed. Therefore, when building the network, we appropriately reduced the proportion of convolutional layers of the 3D-CNN.

In LRCN, it obtained better performance in the two kinds of datasets. The auto-labeled dataset achieved a higher accuracy when they had no preprocessing process, while the manual-labeled dataset had higher accuracy when they underwent preprocessing process. The reason might be that the manual-annotated dataset had a complete lesion region. Therefore, the normalization process stretched the grayscale so that the high and low grayscale interval became more extensive, which improved the network's ability to recognize blood vessels and non-vessels. For the auto-labeled dataset, image preprocessing process also improved the test set's accuracy, but the two preprocessing methods had little difference in test results.

Although the results of the manual-labeled dataset were better than the auto-labeled dataset, the accuracy of auto-location accuracy was also as high as 0.93. In addition, there was no need to annotate the lesion by human, which promoted the automation degree of moyamoya diagnosis.

## 4.5 Summary

In this chapter, we introduced an automatic location detection method for moyamoya lesions. The model, trained by auto-annotation dataset, obtained an accuracy of 93% in diagnosing moyamoya disease, which was close to the results based on manual labelling. Obviously, we can get better performance, if we manually selected the frame which contained the biggest nidus and annotated the ROI to train the network. However, it increases the burden of medical staff, violates the original intention of automatic diagnosis, and cannot be applied to clinical diagnosis.

However, our ROI size was fixed that may not obtain the whole region or even contain useless information. We believed that if we can get more DSA of moyamoya disease, the methods were expected to be applied to clinical diagnosis, and exerted its value.

# 5 Assisted diagnosis of AVM based on radiomics and time phase analysis

## 5.1 AVM Diagnosis

### 5.1.1 Patients and material

Portions of text and figures reproduced from previous work [48]. This retrospective study protocol was approved by the ethics committees of the Huashan Hospital, Fudan University, and informed consent was exempted. From January 2010 to December 2013, 1025 patients with cerebrovascular diseases who underwent DSA examination before operation or conservative treatment were reviewed. The exclusion criteria were as the following: 1) lack of anteroposterior position image, 2) low image quality, and 3) accompanied with other diseases which could be presented in DSA, such as aneurysms, moyamoya disease and brain tumor(Fig.5.1). Finally, among the 153 normal cases, 30 were diagnosed with cavernous hemangioma by MRI, and 47 were diagnosed as aneurysms-negative by DSA and confirmed as spontaneous subarachnoid hemorrhage in CT. 36 cases were negative in DSA anteroposterior position images, but were confirmed as aneurysms in three-dimension rotational angiography(3DRA). 40 cases were suspected of aneurysms by computed tomography angiography(CTA) or magnetic resonance angiography(MRA) but proved to be normal or artery ectasia by DSA(Table5.1). Data collected also included patients' age, gender, and Martin-Spetzler Score [49], etc.

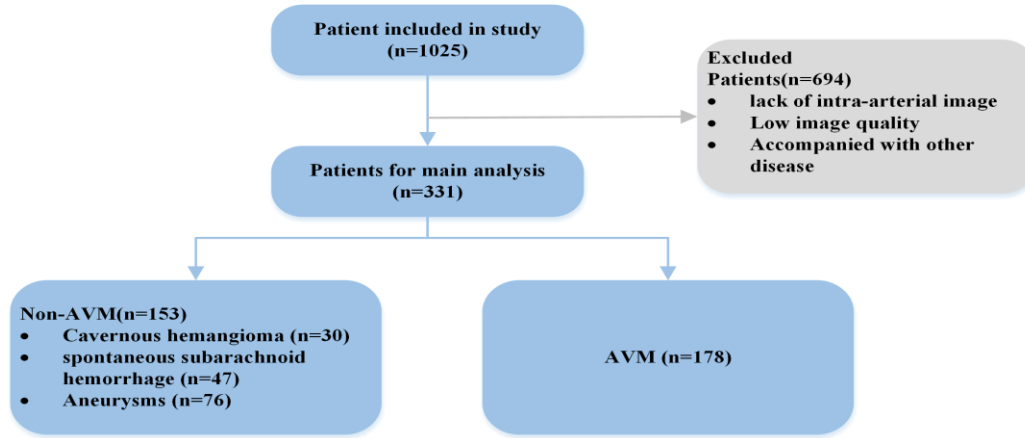


Fig.5.1 The flowchart of patients selection

Table 5.1 Data summaries for diagnosis

| Variables        | Normal      | AVM         | p-value |
|------------------|-------------|-------------|---------|
| Sex(M/F)         | 153(81/72)  | 178(107/71) | 0.189   |
| Age              | 43.72±13.97 | 29.00±13.01 | <0.001  |
| Smoking          |             |             | <0.001  |
| Non-smoking      | 90 (58.8%)  | 136 (76.4%) |         |
| Smoking          | 63 (41.2%)  | 42 (23.6%)  |         |
| Drinking         |             |             | 0.205   |
| Non-drinking     | 114 (74.5%) | 143 (80.3%) |         |
| Drinking         | 39 (25.5%)  | 35 (19.7%)  |         |
| Hypertension     |             |             | <0.001  |
| Non-hypertension | 96 (62.7%)  | 160 (89.9%) |         |
| Hypertension     | 57 (37.3%)  | 18 (10.1%)  |         |

### 5.1.2 Feature extraction

In the previous chapter, we had introduced that the DSA phase can be distinguished by counting the types and orders of cerebrovascular structure in developed frames. According to the detected structures in each frame, the developed structure order can be found easily. Then, we put the original DSA into the model; the model would detect the cerebrovascular structure in each frame. The details of the proposed time-sequence features were summarized in Table 3.2. According to different frame lengths of DSA sequence, we selected five images from developed starts to ends to represent the early arterial phase, later arterial phase, capillary phase and early vein phase, and sinus phase. Three sets of radiomics features were considered here:

1. The radiomics features. A total of 1750 radiomics features, including intensity,

texture, and wavelet features [50,51,52], were extracted from each sample. This group was to evaluate the ability of DSA radiomics to cerebrovascular disease diagnosis.

2. The time sequence feature. This part was to determine the time association among different time phases in DSA.
3. Time sequence features and radiomics features. These two feature sets were concatenated into an integrative dataset and a more accurate model was expected from two types of features that should capture static and dynamic information from the input images.

### **5.1.3 Features Selection and model building**

Since the number of cases was not large, the deep network was prone to overfitting, so we adopted the following method: first, we regarded the combined features set as the experimental group, and the radiomics features set and time features set as the control group. We applied the iterative sparse representation (ISR) for feature selection [53,54]. In each iteration, a proportion of samples were used in training. The average performance of multiple iterations was calculated to get coefficients indicating the importance of the corresponding features. Finally, the SVM was applied to the diagnostic tasks. The specific principles of SVM was introduced in chapter 2. We used leave-one-out (LOO) cross-validation to evaluate the diagnosis model in the experimental group and the control group. Then, the independent validation set was used to assess the diagnostic performance of each model further.

## **5.2 AVM nidus staging**

In clinical diagnosis, it was usually necessary to combine DSA images of multiple positions to judge the AVM's grade. In this part, we tried to reduce the number of positions required for classification as much as possible while ensuring reliability. A total of 178 AVM with anteroposterior position and lateral position images was selected in this study.

First, the proposed time features would be tested in staging task, where the five representative images without annotations were applied. Then, annotated datasets, marking the nidus, supply vein, and drainage vein, were applied to get the optimal model.

### 5.2.1 Patients and materials

The AVM nidus can be divided into five stages, according to the size, the functional area, and the drainage vein. The specific staging indicators and the data summaries were shown in Table 5.2. Determined each property separately, and the sum of the scores was the final grading result. The anteroposterior position (AP) and lateral position(LAT) representative images of the different stages were shown in Table.5.3.

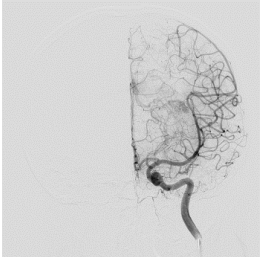
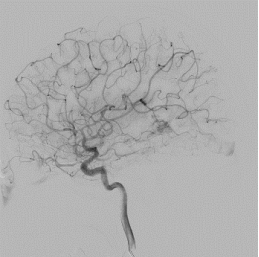
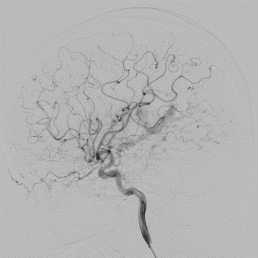
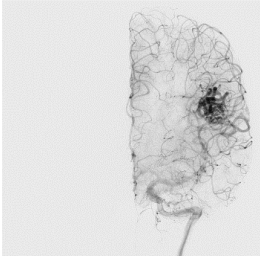
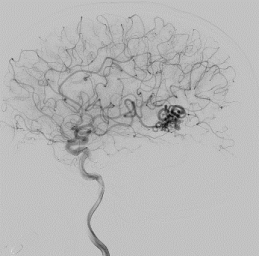
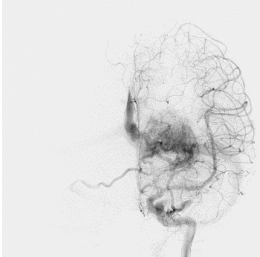
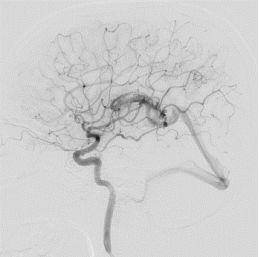
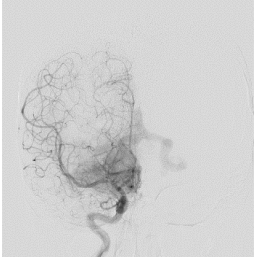
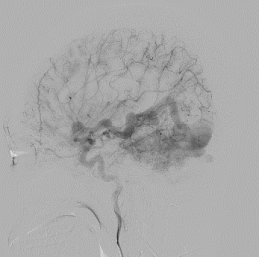
Table 5.2 Data summaries for AVM staging

| Variables                                      | Stage (I,II,III) | Stage (IV,V) | p-value |
|--|------------------|--------------|---------|
| Sex(M/F)                                       | 94 (58/36)       | 84 (49/35)   | 0.647   |
| Age  | 29.12±13.57      | 28.87±12.43  | 0.899   |
| Symptoms                                       |                  |              |         |
| Accidentally found                             | 19               | 16           | 0.846   |
| Headache                                       | 53               | 37           | 0.101   |
| Epilepsy                                       | 19               | 39           | <0.001  |
| Hemorrhage                                     | 43               | 32           | 0.305   |
| Size   |                  |              |         |
| Small (<3cm)                                   | 48 (51.1%)       | 0            | <0.001  |
| Medium (3-6cm)                                 | 43 (45.7%)       | 28 (33.3%)   |         |
| Large (>6cm)                                   | 3 (3.2%)         | 56 (66.7%)   |         |
| Location                                       |                  |              |         |
| Non-situated in neurological<br>critical areas | 54 (57.4%)       | 11 (13.1%)   | <0.001  |
| Situated in neurological<br>critical areas     | 40 (42.6%)       | 73 (86.9%)   |         |
| Deep venous drainage                           |                  |              |         |
| Non-deep venous drainage                       | 49 (52.1%)       | 16 (19.0%)   | <0.001  |
| Deep venous drainage                           | 45 (47.9%)       | 68 (81.0%)   |         |

In Table 5.2, age and cases with hypertension were significantly different between the normal cases and brain AVM patients. Baseline characteristics of patients with lower levels of brain AVM (Stage I,II,III) and higher levels of brain AVM (Stage IV,V) are

presented. More patients with higher levels of brain AVM (Stage IV,V) presented with epilepsy than patients with lower levels of brain AVM (Stage I,II,III) ( $p < 0.001$ ), probably due to the stimulus of larger nidus to cortex.

Table 5.3 Image of different stage

| Stage   | AP  | LAT  | Description   |
|---------|---|--|---|
| Stage 1 |    |    | Less than 3cm;<br>No deep venous drainage;<br>Not at functional area. |
| Stage 2 |   |   | Less than 3cm;<br>Having deep vein;<br>Not at functional area.        |
| Stage 3 |  |  | More than 3cm;<br>Having deep vein;<br>Not at functional area.        |
| Stage 4 |  |  | More than 3cm;<br>Having deep vein;<br>At functional area.            |
| Stage 5 |  |  | More than 6cm;<br>Having deep vein;<br>At functional area.            |

## 5.2.2 Model building with stage

Considering that the data sample was limited, the time features were only applied in the classification task of stage1,2,3 and stage4,5 on five representative images without annotations.

In next part, we selected the frames with the largest lesion area in the anteroposterior position(AP) and the lateral(LAT) position of the internal carotid artery as the research dataset. According to the dataset distribution, we adopted multiple two-class models(Table 5.4) to classify the AVM staging. Because the number of stage1 was too small, it is not considered in an independent classification task. The specific steps were as follows:

1. Built a two-class model on stage1, 2, 3, and stage 4, 5.
2. Built a two-class model on stage 1, 2, and stage 3.
3. Built a two-class model on stage 4 and stage 5.

Table 5.4 The dataset of different classifier

| #            | Stage | Num | Stage | Num | Total |
|--------------|-------|-----|-------|-----|-------|
| Classifier 1 | 1,2,3 | 94  | 4,5   | 84  | 178   |
| Classifier 2 | 1,2   | 49  | 3     | 45  | 94    |
| Classifier 3 | 4     | 45  | 5     | 39  | 84    |

## 5.2.3 Model building with properties

Given that the samples were limited and the sample distribution was very unbalanced, the reliability of classifier chain was getting lower and lower. In clinical, we determined the malformation group's size, the drainage vein, and functional area to calculate the final score. The evaluation rules were shown in Table 5.5. In addition, the nidus size cannot be observed the 2D DSA image, therefore we only considered properties of function area and drainage vein to classification tasks.

Since the sample was the single image of two common positions rather than continuous frames, the temporal features were not helpful to the classification task. However, the

SVM classifier that only was trained by radiomics features did not perform well on the classification tasks of functional areas and drainage veins. We applied the method proposed in the paper [55,56,57], a hybrid features of hand-crafted radiomics (HCR) and deep-learning radiomics (DLR) were integrated in one group, and then selected the features and used SVM for classification. In our work, we applied the VGG16 pre-trained model to extract image features, and then combined the deep features with the radiomics features and formed to one-dimensional vector.

Table 5.5 Data summaries

| Volume          | Property      | Num | Total |
|-----------------|---------------|-----|-------|
|                 | Large(>6cm)   | 46  |       |
|                 | Medium(3-6cm) | 81  | 178   |
|                 | Small(<3cm)   | 51  |       |
| Functional area | Yes           | 116 |       |
|                 | No            | 62  | 178   |
| Vein type       | Deep Vein     | 112 |       |
|                 | Surface Vein  | 66  | 178   |

There were three feature groups we set down. The group 1 was the feature of radiomics, while group2 was the feature extracted from a deep network and the group 3 was a combination of radiomics features and deep features.

1. The handcraft radiomics features (HCR).The radiomics were chosen to describe three main image properties (Table5.6): intensity features(16), wavelet features(280), texture features(54). Finally, a total of 350 radiomics features were extracted in one image.
2. The deep learning radiomics features (DLR).The pre-trained VGG16 network, based on scikit-learn packaged model, was employed to extract deep network features. We resized the image to the size of 224×224 and inputted it into VGG16. Finally, 4096 deep features were extracted from the first fully connected layer (fc1)

in one frame.

3. The combined features (HCR+DLR). The features of (1) and (2) were concatenated into an integrative dataset. A total of 4446 features were obtained.

Table 5.6 The summaries of radiomics features

| Feature name                              | Num |
|---|-----|
| First-order histogram features            | 16  |
| Gray-level co-occurrence matrix           | 23  |
| Grey-level run length matrix              | 13  |
| Gray level size zone matrix               | 13  |
| Neighbourhood gray-tone difference matrix | 5   |
| Wavelet feature                           | 280 |
| Total                                     | 350 |

## 5.3 Results

### 5.3.1 AVM diagnosis results

Accuracy(ACC), sensitivity(SENS), specific(SPEC) were used to evaluate the performance of the classifier. Their definitions were as follows:

$$ACC = \frac{TP + TN}{TP + TN + FN + FP} \quad (5.1)$$

$$SENS = \frac{TP}{TP + FN} \quad (5.2)$$

$$SPEC = \frac{TN}{TN + FP} \quad (5.3)$$

We also calculated the area receiver operating characteristic (ROC) curve to establish the models' overall performance. After feature selection, the features contribution of combined features was shown in Fig.5.2. The red bar represented the time features, while the blue bar corresponded to the traditional static image features that clearly showed that time features took precedence over most radiomics features. Due to the limited data, we used the leave-one-out method for cross-validation, which took one sample as the test set and the remaining samples as the train set in each iteration. When

the optimal model was obtained, we inputted the independent test set into the model for testing. The receiver operating characteristic curve (ROC) of the cross-validation set and the independent test set were shown in Fig. 5.3 and 5.4. The specific performance indicators were shown in Table 5.7.

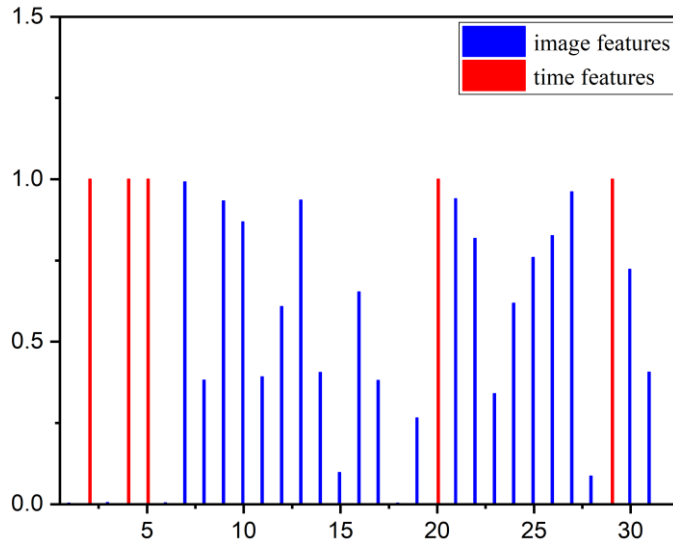


Fig.5.2 The feature distribution of a case. The time features(red bar) and static image features(blue bar)

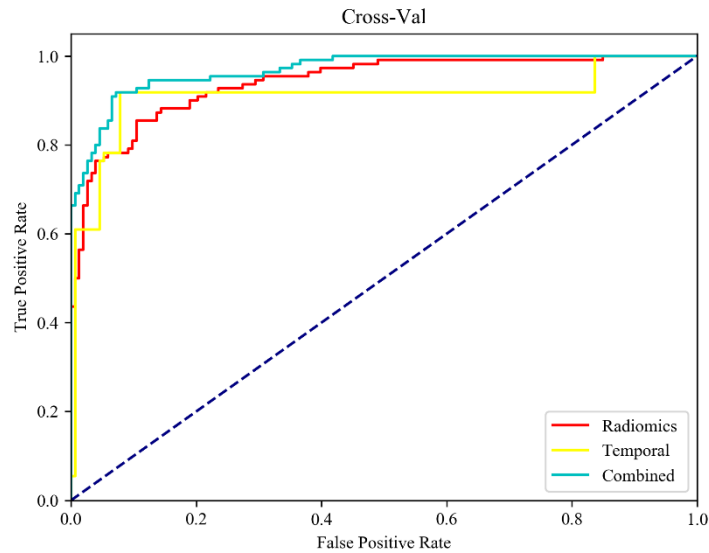


Fig.5.3 The ROC in the cross-validation

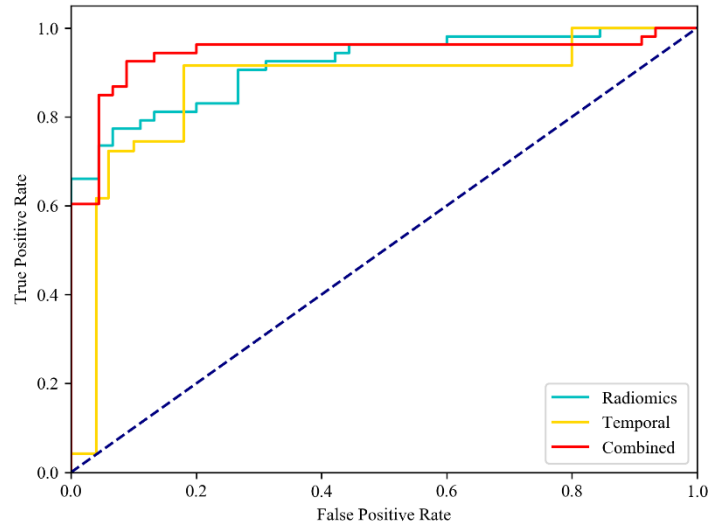


Fig.5.4 The ROC in the independent testing

Table 5.7 The performance comparison of the model trained by different feature sets

|                             | Feature set        | ACC          | AUC          | SENS         | SPEC         |
|-----------------------------|--------------------|--------------|--------------|--------------|--------------|
| LOO cross-validation cohort | Radiomics features | 0.871        | 0.941        | 0.882        | 0.854        |
|                             | Temporal features  | 0.863        | 0.909        | 0.782        | 0.922        |
|                             | Combined features  | <b>0.914</b> | <b>0.968</b> | <b>0.935</b> | <b>0.891</b> |
| Independent testing cohort  | Radiomics features | 0.856        | 0.913        | 0.856        | 0.855        |
|                             | Temporal features  | 0.850        | 0.873        | 0.735        | 0.935        |
|                             | Combined features  | <b>0.909</b> | <b>0.967</b> | <b>0.908</b> | <b>0.909</b> |

The model trained by radiomics features performs poorly on the independent test set, while temporal features showed a surprising performance with only five features. The combined features had high robustness, producing an AUC of 0.967 and an ACC of 0.903 in AVM diagnosis. The results could be understood in this way that radiomics features represented static image features and time features represented dynamic frames relationship. The temporal features with radiomics features can describe DSA video more completely.

### 5.3.2 AVM staging results

This section involved two parts. The first part was an experiment to classify the nidus

directly and verified the effectiveness of temporal features in staging task, and the second part was an experiment to classify the nidus properties.

In the first part, multiple classifiers were established to diagnose the AVM. We used ACC, AUC, SPEC, and SENS to evaluate the performance of each model.

In the second part of the experiment, we did two classified tasks: one was functional areas and non-functional areas, and the other was deep drainage veins and surface drainage veins. Taking the unbalance of each category into account, the Matthews correlation coefficient (MCC), was introduced to evaluate the performance. The calculation formula was:

$$MCC = \frac{TP \times TN - FP \times FN}{\sqrt{(TP + FP)(TP + FN)(TN + FP)(TN + FN)}} \quad (5.4)$$

In first part, labeled images were applied in three models, and the performance indicators of them were shown in Table 5.8:

Table 5.8 The results of staging models

| #           | Stage  | ACC   | AUC   | SPEC  | SENS  |
|-------------|--------|-------|-------|-------|-------|
| Classifier1 | 123/45 | 0.904 | 0.937 | 0.883 | 0.938 |
| Classifier2 | 12/3   | 0.710 | 0.721 | 0.701 | 0.717 |
| Classifier3 | 4/5    | 0.825 | 0.886 | 0.877 | 0.842 |

The results showed that classifier 1 and classifier 2 had good performance indicators, while classifier 3 performed slightly worse. Classifier 1 performed well to classify the first, second, third, and fourth, and fifth stages. The reason might be that the first, second, and third stages were visually separable from the fourth and fifth stages in image morphology. Although classifier 3 was also good, there were only 84 cases of the two categories, and the final result may be the overfitting. It was necessary to increase the amount of data to promote the reliability of the result. The classifier 2 performed worse in the classification of the first, second, and third stage. On the one hand, the difference between the second and third stage was so small that it was difficult to distinguish by the naked eye. On the other hand, some data were ambiguous to

determine in 2D DSA images.

On the classifier1, we used the unannotated images to test the effectiveness of temporal features. The model's indicators with and without time features were shown in Table 5.9. After combining the time features, the indicator had a slight increase. This result proved that the time features had an effect on the grading of the deformity group.

Table 5.9 The comparison of two model

| # | Feature set           | ACC   | AUC   | SPEC  | SENS  |
|---|-----------------------|-------|-------|-------|-------|
| 1 | With time features    | 0.840 | 0.871 | 0.866 | 0.797 |
| 2 | Without time features | 0.801 | 0.867 | 0.754 | 0.830 |

In second part, the summary of the three feature sets was shown in the table below.

Table 5.10 Summary of the three feature set

| Feature Set | Number of features |         |
|-------------|--------------------|---------|
|             | Samples            | Initial |
| HCR         | 178                | 350     |
| DLR         | 178                | 4096    |
| HCR+DLR     | 178                | 4446    |

After filtering the features, we used the leave-one-out cross-validation method to train the SVM. We compared the SVM model's performance on the different feature sets on the functional area(see Table 5.11) and deep vein (see Table 5.12) respectively.

Table 5.11 The result of three feature set in functional area

| # | Feature set | ACC   | AUC   | SPEC  | SENS  | MCC   |
|---|-------------|-------|-------|-------|-------|-------|
| 1 | HCR         | 0.769 | 0.787 | 0.672 | 0.822 | 0.478 |
| 2 | DLR         | 0.795 | 0.838 | 0.688 | 0.780 | 0.551 |
| 3 | HCR+DLR     | 0.863 | 0.933 | 0.828 | 0.881 | 0.702 |

Table 5.12 The result of three feature set on vein

| # | Feature set | ACC   | AUC   | SPEC  | SENS  | MCC   |
|---|-------------|-------|-------|-------|-------|-------|
| 1 | HCR         | 0.687 | 0.743 | 0.581 | 0.750 | 0.321 |
| 2 | DLR         | 0.753 | 0.848 | 0.788 | 0.732 | 0.513 |
| 3 | HCR+DLR     | 0.843 | 0.894 | 0.863 | 0.830 | 0.664 |

Notably, the classifier trained on the feature set that combines deep features and radiomics features had better performance. In two tasks, the DLR indicators were better than those of experimental HCR, which proved that the deep network could extract more useful features than the radiomics method in DSA images. When the radiomics feature was combined with the deep network feature, the indicators of group 3 were higher than those of the DLR. In combined features set, the value of MCC was better than HCR and DLR. Given that the dataset was limited, only two position images were used in this part. In the future, we can consider using more positions for research that may achieve better results.

## 5.4 Summary

In the diagnosis task, we introduced a vascular phase feature extraction method based on deep learning and then fusion with DSA radiomics features, finally proposed an AVM-assisted diagnosis method. The combined features obtained an ACC of 90.9% and AUC of 96.7%.

In the nidus staging task, the classification accuracy between the first, second, third, fourth, and fifth stages was as high as 90.7%. Also, we compared the features set with and without time features in the first classifier, which verified the effectiveness of our proposed features. In nidus properties classification task, the influence of the fusion features on classification was explored on function areas and draining veins. The fusion features got the best performance in all feature groups.

Several limitations should be noted. First, If the nidus is so large, covers the vascular structures, that we have to exclude these samples, it will affect the credibility of the time features extracted by the detection model. Second, in clinical setting, more position

images can increase the diagnosis accuracy by doctors. However, not every patient in our study provides multi-position DSA images. Therefore, we select the limited position images for analysis to diminish the selection bias. Finally, more samples should be collected to provide a more convincing result.

## 6 Conclusion and Future Work

### 6.1 Conclusion

DSA video provides an important basis for the diagnosis of cerebrovascular disease, and also provides a reference plan for surgical treatment, which is of great significance for the study of cerebrovascular disease.

This thesis takes the DSA images of moyamoya disease and AVM as the research object. We explore a time-phase analysis method for DSA video. On this basis, the process for diagnosis of cerebrovascular disease without manual intervention, including the positioning of moyamoya lesions, the differentiation of DSA phases, the diagnosis of AVM, and the AVM staging is proposed, which assists doctors to improve their diagnosis efficiency and accuracy. The main contributions can be summarized as follow:

1. For the study of DSA video, we have introduced a time phase analysis method, based on Faster-RCNN, to provide dynamic temporal features from limited frames. According to the order and type of blood vessels, DSA can be divided into four phases with an average accuracy of 90.8%.
2. In moyamoya disease, the time phase analysis method is applied to locate the moyamoya lesions. The results showed that the ROI obtained by automatic location has achieved accuracy of 93% that is close to manual-location on the same deep network, improving DSA image reading efficiency.
3. In the AVM, we design a model for AVM diagnosis and AVM staging, where the temporal features are integrated with the radiomics features. The results verify that time information is of great significance in DSA diagnosis, and the fusion features can improve the classification accuracy of the model.

---

## 6.2 Future Work

This paper proposes a time phase analysis and radiomics method for DSA video. However, these methods still have shortcomings. The model can be improved from the following perspectives.

1. From the perspective of data sources, we do not include multi-position images to establish the DSA diagnostic model. Although many studies have reported that multi-modality images can help classify tasks, multi-position images are not available for all included patients in the current study. Meanwhile, the number of cases used in this thesis is relatively limited; more data with pathological results need to be collected in the future.
2. DSA is only a two-dimensional image and cannot describe blood vessels' shape and blood flow rate. Combining CTA and DSA images, more comprehensive modeling of cerebral blood vessels can be carried out in the future. The influence of drainage veins and supply veins on the size of malformations also can be analyzed.

# References

1. M.M.Orkisz , C. Bresson , I.E.Magnin ,O. Champin ,P.C.Douek , *Improved vessel visualization in MR angiography by nonlinear anisotropic filtering*.Magnetic Resonance in Medicine,1997, **37**(6):p.914–919.
2. Bash S, Villablanca J P, Jahan R, et al. *Intracranial vascular stenosis and occlusive disease: evaluation with CT angiography, MR angiography, and digital subtraction angiography*. American journal of neuroradiology, 2005, **26**(5):p.1012-1021.
3. J.V. Byrne, *Cerebrovascular malformations*.European Radiology, 2005, **15**(3):p.448–452..
4. Derdeyn, Colin P., et al. Management of brain arteriovenous malformations: a scientific statement for healthcare professionals from the American Heart Association American Stroke Association. Stroke ,2017, **48**(8):p.200-224.
5. Zhao J, Wang S, Li J, et al. Clinical characteristics and surgical results of patients with cerebral arteriovenous malformations. Surgical neurology, 2005, **63**(2):p. 156-161..
6. [Bentoutou, Y., et al. An invariant approach for image registration in digital subtraction angiography. Pattern Recognition, 2002, **35**(12):p.2853-2865.
7. Chilcote W A, Modic M T, Pavlicek W A, et al. Digital subtraction angiography of the carotid arteries: a comparative study in 100 patients.Radiology,1981, **139**(2):p.287-295.
8. Fischer EG. Impaired Perfusion Following Cerebrovascular Stasis: A Review. Arch Neurol. Archives of Neurology,1973, **29**(6):p.361–366.
9. Shi, Zhang et al. Radiomics: Definition and clinical development.Chinese journal of lung cancer, 2019, **19**(6-7):p.385-388.
10. Parekh V, Jacobs M A. Radiomics: a new application from established techniques . Expert review of precision medicine and drug development, 2016,**1**(2):p.207-226..
11. Thawani R, McLane M, Beig N, et al. Radiomics and radiogenomics in lung cancer: a review for the clinician. Lung Cancer, 2018, 115:p. 34-41..
12. Gillies RJ, Kinahan PE, Hricak H. Radiomics: Images are more than images, they are data. Radiology. 2016, **278**(2):p.563–577.
13. Ferreira Junior JR, Koenigkam-Santos M, Cipriano FEG, et al. Radiomics-based features for pattern recognition of lung cancer histopathology and metastases. Comput Methods Programs Biomed. 2018,159:p.23–30.
14. Dalmış M U, Litjens G, Holland K, et al. Using deep learning to segment breast and fibroglandular tissue in MRI volumes. Medical physics, 2017, **44**(2):p.533-546.
15. Yuan M, Zhang YD, Pu XH, et al. Comparison of a radiomic biomarker with volumetric analysis for decoding tumour phenotypes of lung adenocarcinoma with different disease-specific survival. Eur Radiol. 2017, **27**(11):p.4857–4865.
16. M. Anthimopoulos, S. Christodoulidis, L. Ebner, A. Christe and S. Mouggiakakou, Lung Pattern Classification for Interstitial Lung Diseases Using a Deep Convolutional Neural Network. IEEE Transactions on Medical Imaging, 2016, 35(5):p.1207-1216.
17. Huang YQ, Liang CH, He L, et al. Development and validation of a radiomics nomogram for preoperative prediction of lymph node metastasis in colorectal cancer.J Clin Oncol.2016, p.2157–2164.
18. LI Z, WANG Y, YU J. Reconstruction of thin-slice medical images using generative adversarial

- network. International Workshop on Machine Learning in Medical Imaging. Springer, Cham, 2017, p.325-333.
19. 张叙, 高洁, 蔡彦, 李志勇, 基于 DSA 定量评价颈动脉狭窄引起的脑血流灌注功能改变. 第十二届全国生物力学大会, 2018.
  20. Zhang, Y., Zhang, B., Liang, F. et al. Radiomics features on non-contrast-enhanced CT scan can precisely classify AVM-related hematomas from other spontaneous intraparenchymal hematoma types. *Eur Radiology*, 2019, **29**(4):p.2157–2165.
  21. D. Babin, A. Pižurica, L. Velicki, V. Matić, I. Galić, H. Leventić, V. Zlokolica, W. Philips, Skeletonization method for vessel delineation of arteriovenous malformation. *Computers in Biology and Medicine*, 2018, **93**:p.93-105.
  22. Elizabeth Bullitt, M.D., Stephen Aylward, Ph.D., Estrada J. Bernard, Jr., M.D., Guido Gerig, Computer-assisted Visualization of Arteriovenous Malformations on the Home Personal Computer. *Neurosurgery*, 2001, **48**(3):p.76–583.
  23. [23] P. H. Chen, C. J. Lin, and B. Schölkopf, A tutorial on v-support vector machines, *Appl. Stoch. Models. Applied Stochastic Models in Business and Industry*, 2005, **21**(2): p.111-136.
  24. C.J.C.Burges, A tutorial on Support Vector Machines for pattern recognition. *Data mining and knowledge discovery*. 1998, **2**(2):p.121-167.
  25. V. D. Sanchez, Advanced support vector machines and kernel methods. *Neurocomputing*, 2003, **55**(1-2):p.5-20.
  26. C. Campbell, Kernel methods: a survey of current techniques. *Neurocomputing* 2002, **48**(1-4):p.63-84.
  27. Hosmer Jr, David W., Stanley Lemeshow, and Rodney X. Sturdivant. *Applied logistic regression*. 2013.
  28. Breiman, Leo. Random Forests. *Machine Learning*, 2001, **45**(1): p. 5-32.
  29. Cheng, Jie, et al. Improved decision trees: a generalized version of id3. *Machine Learning Proceedings*, 1988, p.100-106.
  30. Quinlan J R. *C4. 5: programs for machine learning*. Elsevier, 2014.
  31. Steinberg D, Colla P. CART: classification and regression trees. *The top ten algorithms in data mining*, 2009, (9): p.179.
  32. Simonyan K, Zisserman A. Very deep convolutional networks for large-scale image recognition. *arXiv preprint arXiv:1409.1556*, 2014.
  33. Kaiming He, Xiangyu Zhang, Shaoqing Ren, et al, Deep Residual Learning for Image Recognition. *CVPR 2016*, p.770-778.
  34. Gers F A, Schmidhuber J, Cummins F. Learning to forget: Continual prediction with LSTM. 1999, p.850-855.
  35. Donahue J, Anne Hendricks L, Guadarrama S, et al. Long-term recurrent convolutional networks for visual recognition and description. *Proceedings of the IEEE conference on computer vision and pattern recognition*. 2015, p.2625-2634.
  36. Tran D, Bourdev L, Fergus R, et al. Learning spatiotemporal features with 3d convolutional networks. *Proceedings of the IEEE international conference on computer vision*. 2015, p.4489-4497.
  37. Carreira J, Zisserman A. Quo vadis, action recognition? a new model and the kinetics dataset. *proceedings of the IEEE Conference on Computer Vision and Pattern Recognition*. 2017, p. 6299-6308.

38. Nunnally T, Chi P, Abdullah K, et al. P3D: A parallel 3D coordinate visualization for advanced network scans, IEEE International Conference on Communications (ICC), 2013, p.2052-2057.
39. Ren S, He K, Girshick R, et al. Faster rcnn: Towards real-time object detection with region proposal networks. *Advances in neural information processing systems*. 2015, p.91-99.
40. Harris C. A combined corner and edge detector. *Proc Alvey Vision Conf*, 1988, **15**(50):p.147-151.
41. Kläser A, Marszalek M, Schmid C. A Spatio-Temporal Descriptor Based on 3D-Gradients. *British Machine Vision Conference Leeds*, 2008.
42. Wang, Heng, Alexander Kläser, Cordelia Schmid, and Cheng-Lin Liu. Action recognition by dense trajectories. *CVPR*, 2011, p.3169-3176.
43. Daniel Costea A, Varga R, Nedeveschi S. Fast boosting based detection using scale invariant multimodal multiresolution filtered features. *Proceedings of the IEEE Conference on Computer Vision and Pattern Recognition*, 2017, p.6674-6683.
44. Dalal N, Triggs B. Histograms of oriented gradients for human detection. *IEEE computer society conference on computer vision and pattern recognition*, 2005, (1): p. 886-893.
45. Felzenszwalb P, McAllester D, Ramanan D. A discriminatively trained, multiscale, deformable part model. *conference on computer vision and pattern recognition*. IEEE, 2008, p. 1-8.
46. Haralick R M, Sternberg S R, Zhuang X. Image analysis using mathematical morphology. *IEEE transactions on pattern analysis and machine intelligence*, 1987,(4): p. 532-550.
47. Sofka M, Stewart C V. Retinal vessel centerline extraction using multiscale matched filters, confidence and edge measures. *IEEE transactions on medical imaging*, 2006, **25**(12): pp.1531-1546.
48. Shi K, Xiao W, Wu G, et al. Temporal-spatial feature extraction of DSA video and its application in AVM diagnosis[J]. *Frontiers in Neurology*, 2021, 12: 651.
49. Mounayer C, Hammami N, Piotin M, et al. Nidal embolization of brain arteriovenous malformations using Onyx in 94 patients. *American Journal of Neuroradiology*, 2007, **28**(3): p. 518-523.
50. Ortiz-Ramón R, Larroza A, Ruiz-España S, Arana E, Moratal D , Classifying brain metastases by their primary site of origin using a radiomics approach based on texture analysis: a feasibility study. *Eur Radiol*, 2018, **28**(11): p.4514–4523
51. Aerts HJ, Velazquez ER, Leijenaar RT et al, Decoding tumour phenotype by noninvasive imaging using a quantitative radiomics approach. *Nature communications*, 2014, **5**(1): p.1-9.
52. Yu J, Shi Z, Lian Y et al, Noninvasive IDH1 mutation estimation based on a quantitative radiomics approach for grade II glioma. *Europe Radiology*, 2017, **27**(8): p.3509–3522.
53. Wu G, Chen Y, Wang Y et al. Sparse representation-based radiomics for the diagnosis of brain tumors. *IEEE Trans Med Imaging* ,2018, **37**(4): p.893–905.
54. Li H, Zhu Y, Burnside ES et al, Quantitative MRI radiomics in the prediction of molecular classifications of breast cancer subtypes in the TCGA/TCIA data set. *NPJ Breast Cancer*, 2016, **2**(1): p.1-10.
55. Spetzler R F, Martin N A. A proposed grading system for arteriovenous malformations. *Journal of neurosurgery*, 1986, **65**(4): p.476-483.
56. Bizzego, Andrea, et al. Integrating deep and radiomics features in cancer bioimaging. *IEEE Conference on Computational Intelligence in Bioinformatics and Computational Biology (CIBCB)*. 2019, p.1-8.

- 56 Li Z, Wang Y, Yu J, et al. Deep learning based radiomics (DLR) and its usage in noninvasive IDH1 prediction for low grade glioma. *Scientific reports*, 2017, **7**(1): p.1-11.

## Published Work

1. **Keke shi**<sup>1</sup>, Weiping Xiao, Guoqing Wu, et al. Temporal-Spatial Feature Extraction of DSA Video and Its Application in AVM Diagnosis. *Front. Neurol.* 12(5).
2. **Keke shi**<sup>1</sup>, Heng Yang<sup>2</sup>, Weiping Xiao<sup>2</sup>, et al. Normal Cerebrovascular Detection and Time Series Classification Based on Faster-RCNN, *Chinese Clinical Neuroscience*, 2020, pp.379-387.
3. Arteriovenous malformation diagnosis system based on DSA.(Software work, 2020SR0813707).
4. Tao Hu<sup>1</sup>, Heng Yang<sup>1</sup>, Wei Ni<sup>2</sup>, Keke Shi, et al. Automatic detection of intracranial aneurysms in 3D-DSA based on a Bayesian optimized filter, *BMEO*, 2020, 19(1):73.
5. Guoqing Wu, Yu Lei, Liqiong Zhang, Wei Ni, Chao Gao, **Keke Shi**, et al. Automatic DSA film reading system with spatial-temporal fusion deep-learning framework and its application in cerebrovascular diseases diagnosis from multiple centers, *Medical Image Analysis*. (Revise).